Optimization of Drying-End-Points Measurements for the Automation of a Fluidized-Bed Dryer Using FT-NIR Spectroscopy

By

Elizabeth Rivera Vázquez

A thesis submitted in partial fulfillment of the requirements for the degree of

MASTER OF SCIENCE

in

CHEMICAL ENGINEERING

UNIVERSITY OF PUERTO RICO

MAYAGÜEZ CAMPUS

2004

Approved by:

---	----------------------------
Federico Padrón Garay, B.S., P.E. Member, Graduate Committee	Date
---	----------------------------
Rodolfo J. Romañach Suárez, Ph.D. Member, Graduate Committee	Date
---	----------------------------
Carlos Velázquez Figueroa, Ph.D. President, Graduate Committee	Date
---	----------------------------
Eduardo Juan García, Ph.D. Representative of Graduate Studies	Date
---	----------------------------
Nelson Cardona Martínez, Ph.D. Chairperson of the Department	Date

ABSTRACT

Automatic control of a fluidized-bed drying process depends on the availability of an in-line sensor to provide accurate measurements of product moisture content. Near-infrared (NIR) spectroscopy technology provides a potentially non-invasive and non-destructive analytical method that could serve as a sensor option for a wide range of applications. The purpose of this research was to investigate the use of NIR spectroscopy for accurate in-line moisture measurements during fluidized-bed drying process and to integrate the NIR set-up as part of drying automation. Five powder mixtures consisting of lactose anhydrous, lactose monohydrate, povidone, blue color additive, and distilled water were dried in a bench-scale fluidized-bed dryer (FBD). Samples were withdrawn from the FBD for the calibration phase. A NIR moisture calibration and validation using partial least squares (PLS) was developed by analyzing statically these samples in conjunction with Karl Fisher Titration. Three probe axial positions were designed and installed in the FBD to take in-line NIR measurements. Due to fluidization effects (segregation and sample density distribution along the bed), a mixed-level factorial experimental design was performed to determine the significance of factors such as mass load, air flow and fiber optic probe axial position in the NIR prediction. The response variable to be analyzed was the residual between in-line measurements and static samples taken immediately after. Data analysis indicated that all factors were significant with residuals ranging from 0.04–2.32. A mathematical correlation was determined to predict future residuals as a function of the operating conditions.

RESUMEN

El control automático de los procesos de secado en lechos fluidizados depende de la disponibilidad de un sensor adecuado que provea medidas precisas sobre el contenido de humedad del producto. La espectroscopía de infrarrojo cercano provee un método potencial, ya que este no es invasivo ni destructivo, y podría emplearse como sensor para una gran variedad de usos. El propósito de este estudio fue investigar el uso de la espectroscopía de infrarrojo cercano para realizar mediciones precisas en tiempo real durante el secado en lecho fluidizado e integrarlo como parte de la automatización. Cinco mezclas de polvos fueron procesados en un secador de lecho fluidizado a escala de laboratorio para extraer muestras estándares y construir un modelo de calibración. Estas mezclas consistían de lactosa anhidra, lactosa monohidratada, povidón, aditivo color azul, y agua destilada. Se desarrolló una calibración y validación de humedad en infrarrojo cercano utilizando el algoritmo de cuadrados mínimos parciales en donde se analizaron estáticamente los estándares conjunto a su valor de titulación en Karl Fisher. Tres posiciones axiales para la sonda de fibra óptica se diseñaron en el secador para hacer mediciones de infrarrojo cercano en tiempo real. Debido a los efectos de fluidización (segregación y distribución de densidad de muestra a lo largo de la camada) fue necesario desarrollar un diseño factorial de niveles mixtos para determinar la importancia de tres factores: grueso de masa, flujo de aire, y posición axial de la sonda de fibra óptica. La variable de respuesta en el diseño factorial fué el residual entre el valor de humedad medido en tiempo real y el valor predicho estáticamente por medio de infrarrojo cercano. El análisis de los datos indicó que todos los factores afectaban significativamente la

predicción con residuales que variaban entre 0.04 hasta 2.32. Una correlación matemática se determinó para poder predecir futuros residuales como función de las condiciones de operación del secador.

Master’s Thesis of Elizabeth Rivera Vázquez
University of Puerto Rico, Mayagüez Campus

Copyright © 2004 by Elizabeth Rivera Vázquez. All rights reserved. Printed in the United States of America. Except as permitted under the United States Copyright Act of 1976, no part of this publication can be reproduced or distributed in any form or by any means, or stored in a database or retrieval system, without the prior written permission of the publisher.

This thesis is dedicated to my family, for their patience and faith. Special mention to my mom Minerva Vázquez, my dad Luis H. Rivera, and Eng. Gustavo Colón for their continuous and unconditional support. Thanks for believing in me. God bless you all.

ACKNOWLEDGEMENTS

Special thanks and warmest gratitude to the ones that, in one way or another, made this achievement possible:

God and my family

Dr. Carlos Velázquez

Dr. Rodolfo Romañach

Prof. Federico Padrón

Dr. Carlos Maldonado

Eng. Gustavo Colón

Mr. Angel Zapata

Mr. Eddie Feliciano

Mr. Alex Rodríguez

Mr. Angel Martínez

Mr. Manuel Popó

Ms. Jesikka Colón

Pharmaceutical Operations Research Group (UPRM)

Chemical Engineering Department (UPRM)

AICHE (American Institute of Chemical Engineers)

AEGIQ (Asociación de Estudiantes Graduados de Ingeniería Química)

INDUNIV – research funding

TABLE OF CONTENTS

List of Figures		x
List of Tables		xii
Chapter I	**Introduction**	**1**
1.1	Justification	1
1.2	Objectives	4
Chapter II	**Literature Review**	**5**
2.1	Near-Infrared Spectroscopy Fundamentals	5
	2.1.1 Historical Issues	5
	2.1.2 Physicochemical Background	6
	2.1.3 Spectral Data Acquisition and Analysis	9
	2.1.4 Applications of NIR Spectroscopy: Previous Works	13
2.2	Fluidized-Bed Fundamentals	16
2.3	Drying Fundamentals	19
2.4	Automation and Process Control Fundamentals	21
Chapter III	**Experimental Set-Up and Procedures**	**23**
3.1	Granules Manufacturing	23
3.2	Near-Infrared Instrumentation and Calibration	25
3.3	Automation and Control Instrumentation Set-up	27

3.4 Mathematical Correlation and Optimization of NIR Measurements 29

Chapter IV Results and Discussion 32

4.1 NIR Calibration Model for Moisture Prediction 32

4.2 Factors Analysis and NIR Optimization Results 38

4.3 ANOVA Results and Regressional Fitting 45

4.4 Implementation of Control Algorithm 50

Chapter V Conclusions and Recommendations 53

References 55

Appendices 62

Appendix A Additional Information for NIR Calibration Model 62

Appendix B Additional Information for ANOVA Analysis 72

Appendix C Additional Information for Application of Control 79

LIST OF FIGURES

Figure 1	Electromagnetic Spectrum	5
Figure 2	Interaction of a light beam on the interface of two media	8
Figure 3	Schematic representation of the PLS regression algorithm	12
Figure 4	Schematic of a batch fluidized-bed dryer	17
Figure 5	Segregation, sample density and particle size distribution in the FBD	19
Figure 6	Typical drying and temperature curves for granulations	20
Figure 7	Schematic of batch control system for the FBD	22
Figure 8	Schematic of fiber optic probe mounting in the fluidized-bed dryer vessel	25
Figure 9	FT-NIR (Vector 22/N) spectrometer external view	25
Figure10	Schematic of the NIR integration in the FBD automation	28
Figure 11	FBD and experimental design schematic	30
Figure 12	NIR absorbance spectra for moisture calibration model	34
Figure 13	NIR prediction vs. true values of moisture content	36
Figure 14	Comparison of NIR prediction vs. true values for test-set spectra	37
Figure 15	In-line and static samples NIR spectra for each experimental set	39
Figure 16	Mass vs. axial position interaction effect for the lowest level of air-flow	40

Figure 17	Mass vs. axial position interaction effect for the medium level of air-flow	41
Figure 18	Mass vs. axial position interaction effect for the highest level of air-flow	41
Figure 19	NIR spectra for 20-30 and 40-45 mesh size samples	43
Figure 20	In-line NIR spectra for a fixed air-flow of 70 m^3/hr and a mass load of 1.0 kg	44
Figure 21	Normal probability plot for predictive model	48
Figure 22	Plot of predicted residuals from Eq. 11 vs. actual residuals from Table 6	50
Figure 23	Graphical user interface and algorithm for the control strategy	51
Figure 24	Comparison of drying curves with moisture values from different analytical sources	52
Figure 25	Air-flow vs. axial position interaction effect for the lowest level of mass load	77
Figure 26	Air-flow vs. axial position interaction effect for the highest level of mass load	77
Figure 27	Process-Pro graphical user interface	80

LIST OF TABLES

Table 1	Most often observed adsorption bands in NIR	7
Table 2	List of ingredients for pharmaceutical formulations	23
Table 3	Data of sample's moisture content for NIR calibration model	33
Table 4	Comparison of pre-treatments effects in the NIR calibration model	35
Table 5	Rank's effect on the statistical of the final regression model with no outliers	38
Table 6	Prediction residual data for experimental design analysis	46
Table 7	ANOVA summary for the mixed-level factorial design	47
Table 8	List of coded factors used in the predictive model	48
Table 9	Summary of NIR prediction residuals using the predictive model of the experimental design	49
Table 10	Cross-validation report for the NIR model using 48 samples	62
Table 11	Calibration report for the NIR model using 48 samples	64
Table 12	Cross-validation report for the NIR model with no-outliers	66
Table 13	Calibration report for the NIR model with no-outliers	68
Table 14	Opus software specifications for the NIR acquisition of spectra	70
Table 15	ANOVA relations for three factors factorial design	72
Table 16	ANOVA report for full mixed-level factorial using all factors	72
Table 17	ANOVA report for full-mixed level factorial using only significant factors	74

Table 18	In-line and static NIR raw moisture data for experimental design	78
Table 19	List of equipment for the instrumentation and control panel	79

CHAPTER I: INTRODUCTION

1.1 Justification

One important issue of pharmaceutical products, especially in solid dosage forms, is the moisture content of the product. The final granule or powder moisture content in a tablet is an essential parameter to describe the properties of a tablet. Moisture influences the intermolecular forces between solid particles in several ways; it may absorb on the surface and influence the surface energy, it may alter the surface conductivity and the electrostatic charging of particles, or it may condense in the capillary regions contiguous to the true areas of contact (Cook and Dumont, 1991). The moisture content in granules affects the stickiness of the tablet surface to the punch and, consequently, alters the tablet surface properties with regard to film coating. The water remaining within the granules affects also the microbiological stability of the tablet produced.

The production of coated tablets, which are among the most usual pharmaceutical delivery forms, typically includes several steps such as blending, milling, granulation, drying, pressing, etc. The process involves physical transformations from the initial powder (or variable granularity) to cores and may also include coating of tablets. Usually, samples are taken from drug substances or drug product batches and analyzed in remote laboratories. The sample goes through stages of documentation, sample preparation, data analysis and documentation once more, prior to reporting the analytical results. For example, the state of water in solid materials may be characterized thermal analysis, Karl Fisher titration and loss-on-drying (LOD), among others. These techniques are not only time consuming but may be subject to errors induced by sampling methods.

Quality control in pharmaceutical industry involves analyses of raw material, intermediate products, and end products. Analyses for intermediate products allow the production process to be monitored and potential malfunctions to be corrected before the end-product is reached. Because quality controls of intermediate manufacturing products and end-products are important on an industrial level, there is a growing interest in developing methods for analysis involving minimal sample preparation.

Typically, fluid-bed dryers are used in the pharmaceutical industry for the drying step of granules. Drying is controlled by using empirical models with easily measurable parameters, such as temperature of the exhaust air, that give an indication of the moisture content of the powder. These methods are susceptible to external influences such as ambient temperature which could distort the relationship significantly. For example, in the summer, when ambient temperatures are higher, the relative humidity of the process air will naturally be higher than in the winter, when the air is cooler. Hence, the product moisture level may vary between batches even though the drying has been stopped at the same temperature, and additional sample testing in the lab is required to ensure product is within specification.

Real-time moisture measurement has become one of the main concerns for industrial processes in which a product is dried or moisturized. Automatic process control of a dryer depends on the availability of an in-line sensor to provide a continuous measurement of product moisture content. Near-infrared (NIR) spectroscopy technology has been developed over the last twenty years for a wide range of industrial applications and is now recognized as an extremely powerful measurement technique for automation and control.

NIR analysis has steadily grown in popularity because of its ability to quickly provide qualitative and quantitative information of many products (Wetzel, 1983). The non-invasive and non-destructive features of vibrational spectroscopy techniques, such as NIR, make them novel tools for in-line quality assurance.

The process control and end-point detection of pharmaceutical dried granulation has traditionally been based on direct, off-line measurements. The aim of this study was to investigate the use of NIR spectroscopy for in-line moisture measurements during fluidized-bed drying process, and further, to integrate the NIR set-up as part of drying automation. Moreover, this study extended to an optimization problem by finding a correlation for the NIR sensor axial positioning with respect to the bulk mass of granulation inside the fluid-bed dryer and fluidization airflow.

To determine if NIR spectroscopy is an alternative for fluid-bed dryer automation, many factors were considered. Sample composition, particle size, homogeneity and temperature variations were some of the so called internal factors. All these factors belong to the substance being analyzed and can be controlled and fixed in the calibration phase of the NIR instrument. Other factors, such as the fluid-bed dryer air-flow, NIR fiber optic probe positioning inside the vessel, and bulk mass inside dryer are external factors related to the medium where the sample is being analyzed. These factors were studied in this investigation.

1.2 Objectives

The goal of this study was to investigate the feasibility of using NIR spectroscopy for in-line moisture measurement and process control during fluidized-bed drying of pharmaceutical powders. The specific targets were:

- To implement the use of a NIR calibration model developed with static samples, to predict in-line moisture samples inside a dryer vessel.
- To build-up a statistical analysis for the probe axial position as a function of fluidization velocity and bulk mass height.
- To understand the effect of physical factors on the in-line moisture measurements with NIR spectroscopy.

CHAPTER II: LITERATURE REVIEW

2.1 Near-Infrared Spectroscopy Fundamentals

2.1.1 Historical Issues

The history of near-infrared (NIR) spectroscopy started with the studies by Herschel (1800). In 1890, Herschel was credited for his discovery and the region from 700 to 1100 nm is often referred as the "Herschel's region". Years later, the American Society of Testing Materials (ASTM) defined the region of NIR spectrum from 780 to 2526 nm, Fig. 1. However, it was not until the 2nd World War that the development of NIR instruments enabled the practical applications of this region of the electromagnetic spectrum (EMS).

Figure 1. Electromagnetic spectrum

The NIR spectrum is just above the visible region of the EMS. This portion of the EMS has for the past 30 years been studied and investigated in great detail as an analytical procedure for the analysis of many natural and man-made materials (McDonald and Prebble, 1993, Siesler et al., 2002, Sinsheimer and Poswalk, 1968, Wetzel, 1983, Workman, 1999a). The actual NIR analysis was developed in the 1950's by a work of a group at USDA (United States Department of Agriculture), headed by

Osborne et al. (1993). They discovered that the non-destructive NIR spectra of biological samples could be obtained with no sample preparation and in less than a minute. This gave rise to a wide range of uses of NIR in the agricultural industry.

Many types of industries have also used NIR for several applications. The petrochemical, pulp and paper, and pharmaceutical industries have taken advantage over characteristics of NIR (Workman, 1999a). Today, more papers are being written about the application of the NIR spectral region to all types of analyses than ever before.

2.1.2 Physicochemical Background

Next to the mid-infrared, the NIR region covers the interval between 4000 - 12,500 cm^{-1} (0.8 – 2.5 μm). Molecules that absorb NIR energy vibrate in two fundamental modes: stretching and bending. Stretching is a continuous change in the inter-atomic distance along the axis between two atoms and it occurs at lower wavelengths than bending vibrations. A bending vibration is a change in the bond angle between diatomic molecules.

The NIR bands are mainly overtones and combinations of fundamental vibrations in the mid-infrared. The most often observed bands in the NIR include combination bands, second and third overtones all attributed to information from the mid-IR.

Table 1 compiles some of the most observed absorptions in this region (Osborne et al., 1993, Reeves, 1994). In connection with O-H absorptions, one of the major applications of NIR spectroscopy is the determination of moisture in food analysis.

Some other absorption bands for water in NIR can occur at 760 nm, 970 nm and 1450 nm (Buijs and Choppin, 1963, Curcio and Petty, 1951). A band observed at 1940

Table 1. Most Often Observed Adsorption Bands in NIR

Bond	**Wavelength (nm)**	**Description**
C-H	2000-2400 1000-1200	aliphatic hydrocarbons
	1620-2100	olefinic
	1650-2207	epoxides
N-H	1500-2000	epoxy-amines
	1446-1492	aromatic amines
O-H	1000-1400	alcohols
	1440-1940	water

nm is known to be caused by O-H stretching and bending vibrations, and is the most used for analytical applications (Choppin and Buijs, 1963, Osborne et al., 1993). These bands have also been applied for high moisture systems (Reeves, 1994). It has recently been reported, from measurements on silica gel layers, that water content has an effect on NIR absorption at all wavelengths, even where water absorbed minimally (Fong and Hieftje, 1995).

Usually, for a solid sample, the reflected light is the parameter measured in NIR spectroscopy known as diffuse reflectance. The incident beam of light can be divided into two forms as shown on Fig. 2; namely the absorbed light and the reflected light. The reflected light consists of two components: specular and diffuse.

The specular (mirror like) component in the boundary between two media occurs at the sample surface and it contains little information about the chemical composition of the substance. The NIR spectroscopy is particularly based on the diffused component of the reflected light and it can be affected by particle size and shape distributions, bulk density, surface characteristics and temperature (Siesler et al., 2002, Wetzel, 1983).

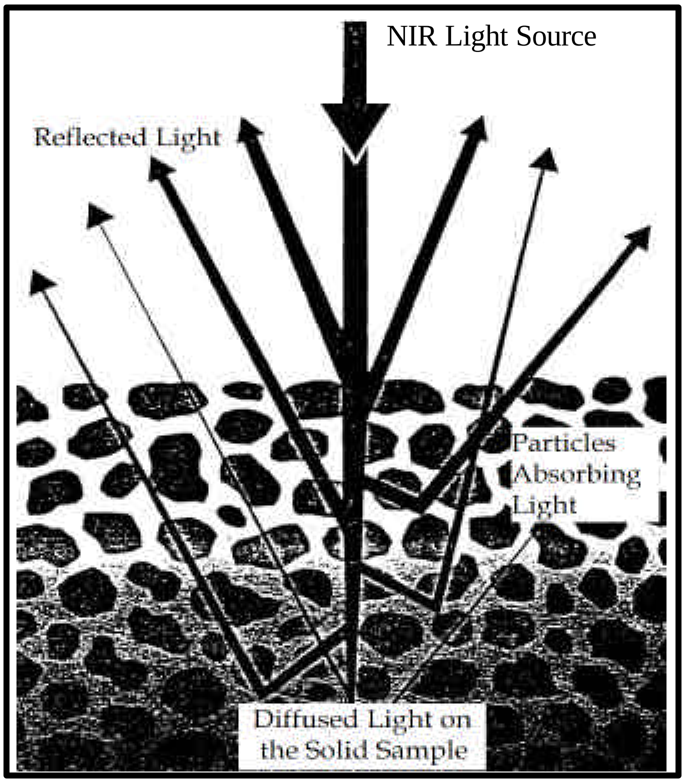

Figure 2. Interaction of a light beam on the interface of two media (Modified from Wetzel, 1983)

Norris et al. (1983) evaluated the particle size effect with wheat. Berntsson et al. (1999) evaluated practical ways to determine effectively the sample mass per unit area. Sample sets studied by Blanco et. al. (2000) revealed different spectral features on batches of blended, core and coated tablets.

The diffuse reflected light is emerged by random reflections, refractions and scatter inside the sample. The exact path of the propagation of light is extremely difficult to model. In practical applications, the apparent absorbance *A* may be applied:

$$A = \log \frac{1}{R} \tag{1}$$

where *R* is the reflectance of the sample. Equation 1 is expected to be related to the concentration of the absorbent.

Diffuse reflectance spectra do not perfectly obeys Beer's law and it can often be linearized by using the Kubelka-Munk function:

$$\frac{K}{S} = \frac{(1-R)^2}{2R} \qquad (2)$$

where R is the diffuse reflectance of the sample, while K and S are absorption and scattering coefficients, respectively. Equation 2 suggests that R decreases as K increases for a constant S, and for a constant coefficient K, the reflectance R increases as scattering S increases (Pasikatan et al., 2001).

The chemical information in the diffusely reflected light is expressed in K, whereas the particle size information is expressed in S. The scattering coefficient is a function of particle size d, that increases in proportion to Eq. 3. This coefficient is also inversely proportional to the mean path length, l.

$$S \; a \; \frac{1}{d} \; a \; \frac{1}{l} \qquad (3)$$

From Eqs. 2 and 3, as d increases S decreases and radiation penetrates deeper into the powder, thus increasing absorbance while reducing the diffuse reflectance. As d decreases, light encounters more scattering boundaries and a reduction in the penetration (S increases). The probability of absorption reduces and the reflected component becomes higher.

2.1.3 Spectral Data Acquisition and Analysis

The bands in the NIR region require that the calibration equation must be constructed using multivariate calibrations, being partial least squares (PLS) the most used one. Multivariate techniques for quantitative work have been covered intensely by several books and papers (Callis et al., 1987, Forina et al., 1998, Hassel and Bowman, 1998, Siesler et al., 2002). Only an abbreviated description is presented in this part. A more in-depth discussion can be found elsewhere.

Nomikos and McGregor (1995) reported a pioneering work on multivariate statistical procedures for monitoring the progress of batch processes. They used PLS to extract information from processes measurement in which time series of nine process parameters were used to model the resulting product properties. This kind of methodology was extended by Wold et al. (1998) using local process time instead of product properties.

For spectral data, all wavelengths which are correlated to the parameter of interest are selected for the PLS method. Equation 4 shows the general calibration equation:

$$C = a\,A + E \tag{4}$$

where ***C*** is the concentration matrix, ***A*** is the matrix of spectral data, ***a*** is a matrix of coefficients, and ***E*** is the matrix of residual error related to the model ability to predict the calibration absorbances. When performing a PLS calibration, the spectral data is reduced to a set of eigenvectors and scores (weighting values for all the calibration spectra) which are related to the parameter of interest. The matrix ***A*** is reduced to only a few factors as explained by Forina et al. (1998). In this way, the spectral noise and random instrument errors are reduced with the discarded part of the information. This approach is used on Eq. 4 instead of the absorbance.

The main advantage of this method is that PLS is more robust than any other multivariate calibration method, and allows the detection of spectral outliers. A PLS regression is useful with small populations of samples that contain some experimental noise in the NIR spectra.

The number of PLS vectors used is defined in the spectroscopic analysis program by the size of the "rank" or number of factors considered in the regression model. The first factor explains the most drastic changes of the spectrum.

The residual (*Res*) is the difference between the true (y_i) and the fitted value (y_f). Thus, the sum of squared errors (*SSE*) is the quadratic summation of these values.

$$SSE = \sum \mathrm{Res}^2 = \sum (y_i - y_f)^2 \tag{5}$$

The root mean square error of estimation *RMSEE* is calculated from this sum, with *M* being the number of standards and *P* is the rank:

$$RMSEE = \sqrt{\left(\frac{1}{M-P-1} * SSE\right)} \tag{6}$$

The correlation coefficient (R^2) gives the percentage of variance present in the true component values, which is reproduced in the regression. R^2 approaches 100% as the fitted values approach the true values:

$$R^2 = \left(1 - \frac{SSE}{\sum (y_i - y_m)}\right) * 100 \tag{7}$$

where y_m is an average of the moisture values. The R^2 can be negative. This is true for low ranks, when the residuals are larger than the variance in the true values. The sum of residuals (*SSE*) decreases with increasing rank, so R^2 approaches a limiting value of 100%.

A cross-validation process is automatically done by the chemometric software in which the program leaves one standard out of the calibration model and predicts it using the model created by the remaining standard. In case of a cross-validation the root mean **s**quare error of cross-validation (*RMSECV*) can be taken as a criterion to judge the quality of the method:

$$RMSECV = \sqrt{\left(\frac{1}{M} * SSE\right)} \tag{8}$$

The calibration is done with the original set of calibration spectra and the test spectra are predicted. In case of a test set validation, Eq. 8 is called the root mean **s**quare error of prediction (*RMSEP*).

PLS simply builds upon the inherent correlation that exists between the spectral data and the constituent concentrations or time based mass loss as applied by Harris and Walker (2000). In effect, this generates two sets of vectors and two sets of corresponding scores; one set for the spectral data, and the other for the constituent concentrations. Presumably, the two sets of scores are related to each other through some type of regression, and a calibration model is constructed as in Fig. 3.

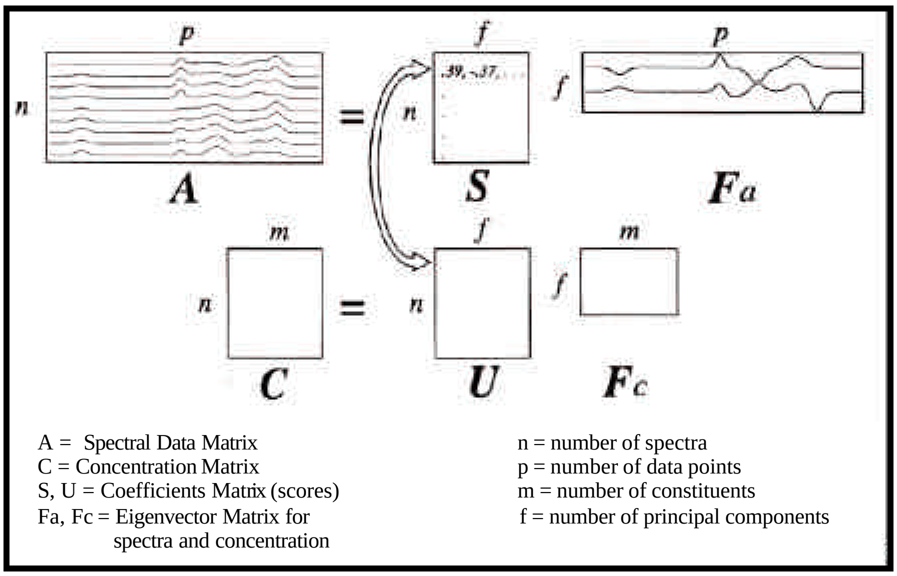

Figure 3. Schematic representation of the PLS regression algorithm(Taken from Duckworth and Springsteen, 1998)

2.1.4 Applications of NIR Spectroscopy: Previous Works

A proliferation of work involving near-infrared spectroscopy in process and image analysis has occurred over the past decade (Wetzel, 1983, Workman, 1999a, Workman et al., 1999b). This review includes the aspects of NIR spectroscopy for the analysis of materials specifically related to pharmaceutical industry.

The limit between process analytical chemistry and the traditional laboratory analysis is quite ambiguous. The terms in-line, on-line, at-line, off-line are often used and referred to in literature. Definitions of these words are given (Callis et al., 1987, Hassel and Bowman, 1998): *in-line*, the sample interface is directly located in the process stream; *on-line*, analysis require automated sampling and sample transfer to an automated analyzer; *at-line*, sampling is completely manual and transported to analyzer located near the manufacturing area; and *off-line*, requires manual sampling and transportation to remote or centralized laboratories for further studies.

Since 1968, the measurement of water was one of the first pharmaceutical applications of NIR (Sinsheimer and Poswalk, 1968). Recently, Derksen and collaborators (1998) improved the efficiency in the search for a suitable specification for the residual moisture content in freeze-dried products in glass vials. They observed offsets in the reflectance spectra caused by variations in particle size, compaction of the sample, and optical aberrations in the glass vials. It was also found that for freeze dried samples some bands shift to a higher wavelength at increasing moisture content, making a PLS regression preferred over single or dual wavelength calibration methods. Moreover, Bertnsson et al. (1997) applied NIR in an at-line process to determine moisture content in bulk hard gelatin capsules and compared multiple linear regression

(MLR) to PLS, being the latter the more robust and able to detect outliers. On the other hand, Miwa and co-workers (2000) developed a method to find suitable amounts of water in granulations. For this study, saturation absorption capacity was characterized by inflection points in plots of NIR output value (at a fixed wavelength of 1.94 μm) against the amount of water added for each excipient.

There are so far a limited number of reports on in-line analysis by NIR in fluidized-bed processes. Frake et al. (1997) demonstrated the use of NIR for in-line analysis of the moisture content in 0.05-0.07 mm pellets during spray granulation in a fluid-bed. Rantanen et al. (2000) described a similar approach for moisture content measurement using a rationing of 3-4 selected wavelengths. In 1998, he and his co-workers reported that the critical part of in-line process was the sight glass for probe positioning that was continuously blown with heated supplied air. They also reported spectra baselines caused by particle size and refractive properties of the in-line samples; they recurred to analyze several data pre-treatments to eliminate these effects on their fixed wavelength set-up.

Solvents other than water have also been evaluated for real-time quantification. Harris and Walker (2000) monitored the vacuum line of a dryer using fiber optic-coupled acoustic-optic tunable filter near-infrared (AOTF-NIR) spectrometer. In this application, a balance was used in the dryer to detect the mass loss of solvent, which was correlated to the spectra collected.

Quantitative studies to investigate the potential of NIR spectroscopy for at-line processes of film coating applied to tablet cores have been reported. Kirsch and Drennen (1996) reported that sample positioning in NIR was a critical concern causing shifting of spectral baselines which interfered with the calibration development. A novel approach was made by Buchanan et al. (1996) for film coating process to study the amount of the active drug contained in a coated tablet. It was determined to ±4% of the target value using both PLS and MLR, and showed that PLS have more accuracy and reliability with HPLC methods.

On-line measurement has also been possible enabling monitoring of film coating on pharmaceutical pellets in an industrial manufacturing process. Andersson et al. (2000) conducted measurements on solid coated tablets using a fiber-optic probe positioned inside a fluidized-bed process vessel. In this case they secured a representative sampling during processing by using a sample collector that was emptied with compressed air inside the vessel.

Tablet hardness tests using NIR methods have been conducted to predict the effects of compression force by Morisseau and Rhodes (1997). Different formulations using five to six levels of tablet hardness from 2 to 12 kg resulted in a prediction at least as precise as laboratory testers. They found that a harder tablet has a smoother surface, thus less diffuse reflectance and higher absorbance was the response regardless of the drug.

NIR spectroscopy was evaluated by Hailey et al. (1996) as an on-line technique to show results as meeting conformance rather than absolute quantitative values during blending process. An NIR probe was interfaced to V-blending vessel at the point of rotation while the blender was operated in a discrete stop-start fashion with the spectral acquisition being triggered when the blender was stationary. Furthermore, a model mixture was used by Sekulic and collaborators (1996, 1998) to evaluate the information content of the data collected using qualitative approaches such as standard deviation, dissimilarity calculations and principal component analysis (PCA) as a mean to determine the blending end-points.

Popó et al. (2002) employed also a lab-scale V-blender to determine drug content in samples collected at various mixing times. In this case they developed a PLS model validated using UV spectrometry.

Finally, the principles of multivariate calibration for NIR diffuse-reflectance spectroscopy have been demonstrated for quantification of active compound and major excipients (Forina et al., 1998). Blanco et al. (2000) applied an at-line application using a fiber optical probe presented as an analytical tool for pharmaceutical preparations at different steps of production process. The active compound, otilonium bromide, was determined at three stages of production (blended product, cores, and coated tablets) to develop a single calibration model for the analyses of the three forms without the need to run an individual calibration for each step.

2.2 Fluidized-Bed Dryers Fundamentals

Small batch fluid-bed dryers, Fig. 4, are commonly used for pharmaceutical powder drying processes (Botterill, 1975, Gelperin and Einstein, 1972, Wu and Baeyens, 1998). According to the type of the material, appropriate fluidized-bed systems are chosen (Dittman, 1977, Mujumdar, 1987). Due to better air-solid contact, drying in fluid-bed dryers is faster than in tray ovens and because of good mixing, product uniformity is much improved. After drying the air is filtered, usually in multicyclones and/or bag

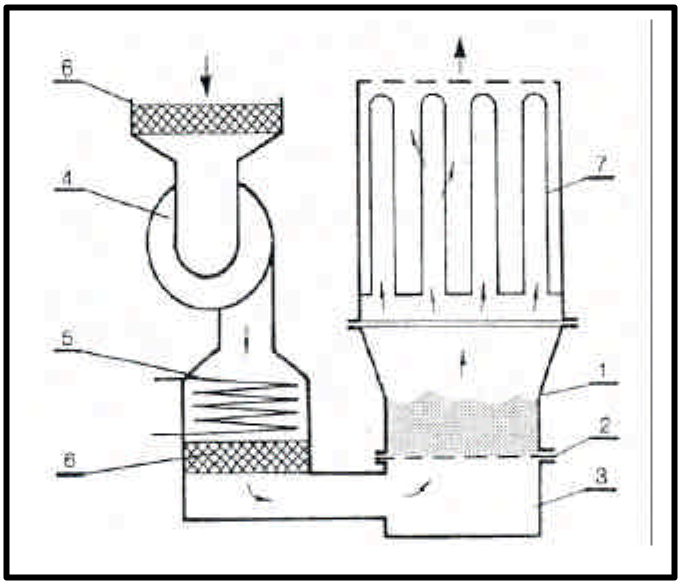

Figure 4. Schematic of a batch fludized-bed dryer : (1) vessel or chamber, (2) gas distributor, (3) plenum chamber, (4) blower, (5) heater, (6) filters, (7) dust collector. (Taken from Mujumdar, 1987)

filters. The use of bag filters is, however, troublesome if the dryer is often used for different products as it requires careful cleaning.

A fluidized bed is essentially non-homogeneous. This is specially the case of the dispersive phase in a gas. A bed may be well fluidized if all the particles are fully supported by the gas, but may still be segregated in the sense that particles with lower density will migrate to the surface whereas those with higher density will migrate to the distributor base. Many models have been proposed to predict the axial distribution of particles with different sizes in a fluidized-bed (Asif, 2002a, Asif and Ibrahim, 2002b, Barghi et al., 2003, Epstein and LeClair, 1985, Gibilaro et al., 1985, Keith, 1980). For example, the counteracting mechanism of convection and dispersion in FBD containing a mixture of solid particles was presented first by Kennedy and Bretton (1966):

$$-D_i \frac{dC_i}{dz} = U_{pi} C_i \tag{8}$$

where D_i is the dispersion coefficient of the *ith* particle species, C_i is its concentration and z is the axial distance. Minor variations in the definition of the particle velocity U_{pi} still continues to be the most widely used approach to describe the mixing and segregation behavior of multisize mixture of solid particles.

Tanfara and colleagues (2002) used electrical capacitance tomography (ECT) to generate contour plots of a fluidized bed cross-sectional area and the wide distribution of placebo granules revealed two different types of gas flow: annular and centralized. They concluded that as the gas velocity was increased a shift from a predominantly annular flow of gas to a centralized core gas flow is likely due to segregation of the large particles near the bottom of the bed. Moreover, their findings were corroborated using the studies of Wu and Baeyens (1998) for the calculation of optimal fluidization velocity for complete mixing of particles. Wu and Baeyens defined a diameter ratio d_r, as the ratio of the mean diameter of the larger particles to the smaller particles. For values of d_r larger than 2, excess gas velocities of the minimum fluidization velocity were needed for complete or good mixing of particles during fluidization.

Asif and Petersen (1993) made their contribution regarding dynamic behavior of particles in fluidized beds. Their study accounted for the presence of density gradients in the mass balance formulation to obtain the concentration profiles throughout the bed. A plot comparison showed that the total volume fraction of particles decreased with height. Figure 5 illustrates the relationship between the fluidization process inside the vessel and the effects on the drying powders.

The gas fluidized bed is characterized by having good heat transfer properties between the fluidized layer and heating or cooling surfaces and extensive work has been done in order to develop equations for the estimation of the heat transfer (Botterill, 1975, Gelperin and Einstein, 1972, Zabrodsky, 1966). Heat transfer is strongly

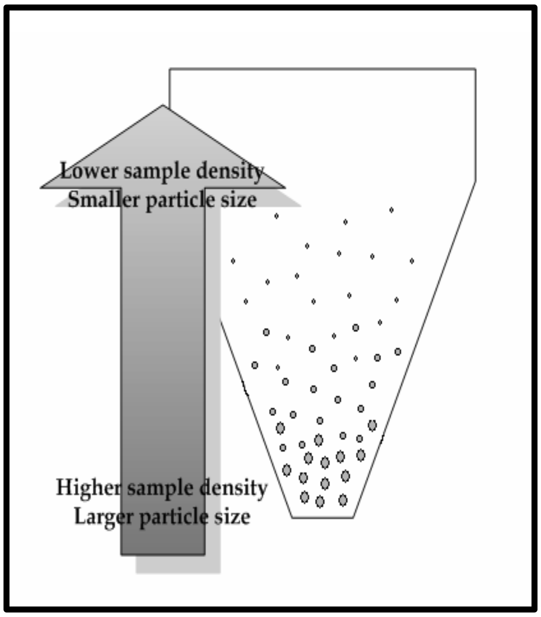

Figure 5. Segregation, sample density and particle size distribution in the FBD

dependent on the heat transfer capacity of the particles and the degree of particle circulation at the heat transfer surfaces because of rising gas (Alvarez and Shene, 1996, Baker, 1999, Langrish and Harvey, 2000, Wang and Chen, 2000). The heat transfer coefficient for wall-to-bed heat transfer increases dramatically when the bed is transferred from a fixed-bed to a fluidized-bed with rapid particle mixing.

2.3 Drying Fundamentals

Drying curves are usually employed for drying test by plotting residual data against time. A typical drying curve is shown in Fig. 6, together with the associated product temperature curve measured during a batch fluid-bed drying test. Morris et al. (2000) summarized two stages (constant drying rate and falling drying rate) during the fluid-bed drying process using two simple relations. The dependence of moisture content *M* with time is linear for the constant drying rate:

$$M = M_o - kT \tag{9}$$

where k is a constant at a given temperature, gas density, bed height and heat of vaporization. The falling drying rate stage is exponential:

$$M = M'_o k.\exp(-k'T) \tag{10}$$

where k and k' are geometric constants summed over n terms in a infinite series. The constant drying rate is also influenced by the air rate, solids hold up and particle size and air temperature is the principal variable influencing the falling drying rate and the equilibrium moisture content (Srinivasa et al., 1995). However, at lower moisture content, drying is controlled by the rate of diffusion of moisture inside the particles and the drying rate is decreased considerably (Wang and Chen, 2000).

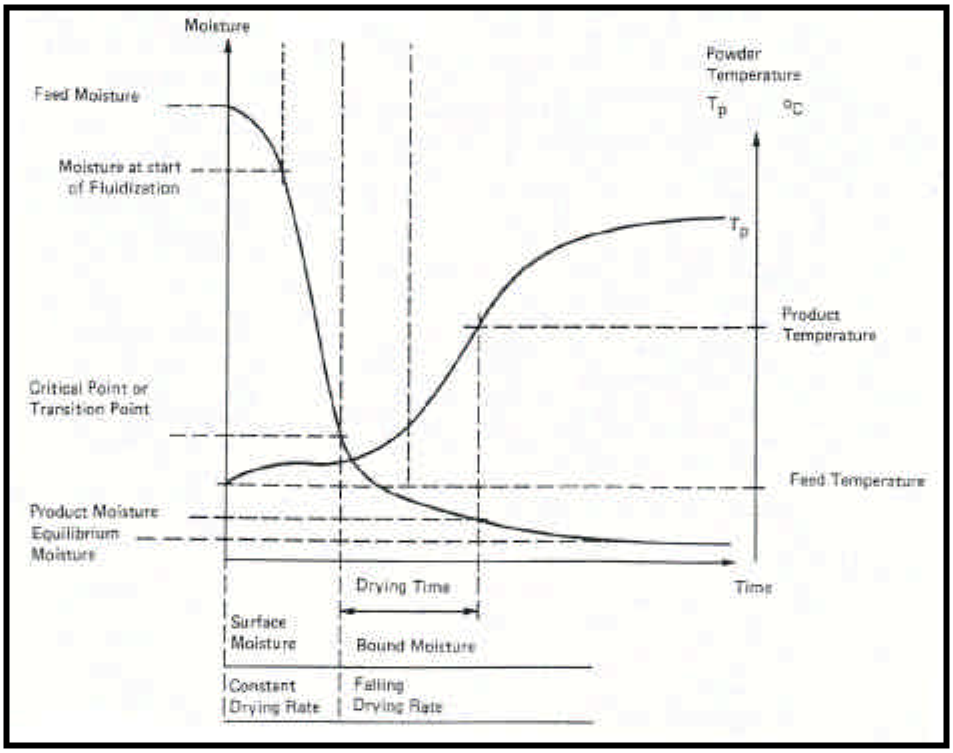

Figure 6. Typical drying and temperature curves for granulations (Taken from Mujumdar, 1987)

2.4 Automation and Process Control Fundamentals

Batch and semi-batch processes, those with discontinuous feed and product stream flows, are used in preference to continuous flow units when relatively small amounts of products are required (Seborg et al., 1989, Smith and Corripio, 1997).

Dynamic models of chemical processes invariably consist of one or more differential equations often combined with one or more algebraic relations. For process control problems, a dynamic model can be obtained from the application of unsteady-state conservation relations, usually material and energy balances. Algebraic equations in the process model can arise from thermodynamic and transport relations.

Automatic process control can be achieved by using a control system. The design and implementation of a possible batch control system is shown on Fig. 7. This type of control strategy is known as feedback control. The three basic components of all control systems are: (1) Sensor/transmitter – for the special case example on Fig. 7, the sensor is the NIR spectrometer that serves as a moisture analyzer, (2) Controller – it is the brain of the control system and it is composed of the PC's that receives the NIR signals, and (3) Final control element – on Fig. 7 this is represented with an on/off switch relay.

These components perform three basic operations that must be present in every batch control system. These operations are: (1) Measurements – measuring the moisture variable done by the sensor and then it is sent to the PC, (2) Decision – based on the measurement, the PC control algorithm decides what to do to reach its desired value, and (3) Action – as a result of the controller's decision, the system sends a signal to the switch relay and order it to continue or to interrupt the drying process.

In the special case of fluidized-bed dryers, automation is typically attained by controlling easily measurable parameters that give an indication of the moisture content of the powder. For example, Szenmarjay and collaborators (1996) used flow rates, temperature and relative humidity in conjunction with enthalpy and mass balances as input data to calculate the desired characteristics of the product. A similar approach has been given by Liptak (1998) but with the use of Shinskey's model. In addition to these parameters, Siettos et al. (1999) incorporated the use of the fuel flow rate of the burner in an industrial system to develop a comparative analysis between a fuzzy logic system and a PID controller.

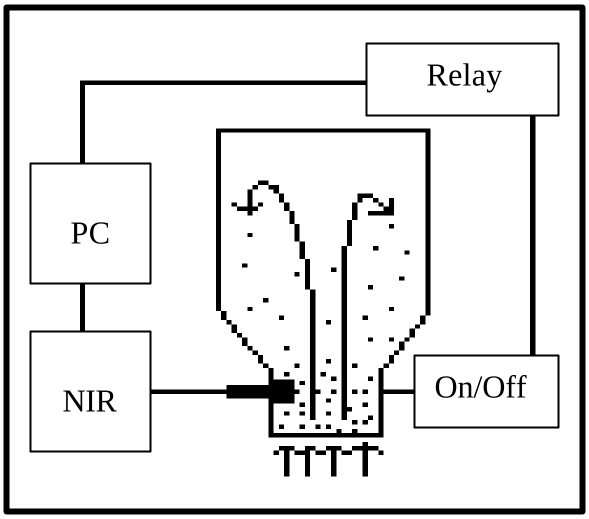

Figure 7. Schematic of a batch control system for the FBD

CHAPTER III: EXPERIMENTAL SET-UP AND PROCEDURES

The procedures performed on this work were divided into four main sections: the manufacturing of pharmaceutical granulations, the near-infrared calibration and set-up, the automation of the fluidized-bed dryer, and the optimization of the on-line near-infrared measurements. This chapter is divided according to these topics.

3.1 Granules Manufacturing

The materials listed on Table 2 are the ingredients used in the preparation of the pharmaceutical granulations. The mixtures were composed of typical tablet excipients. The materials employed were lactose monohydrate (Mutchler™ tabletosse 80/meggle), lactose anhydrous (Sheffield™ product 5X59009), povidone (ISP™ product 1001), blue color additive (Warner-Jerkinson™ Blue No.1), and distilled water. The proportions of each component are shown on Table 2.

Table 2. List of Ingredients for Pharmaceutical Formulations

Ingredient	Amount/batch (g)	% (w/w)
Lactose Anhydrous	2792.5	69.8
Lactose Monohydrate	653.5	16.3
Povidone	47.0	1.2
Blue Color Additive	7.0	0.2
Distilled Water	500.0	*12.5

*Variable during NIR calibration phase

Granulations were performed on a mixer/granulator (LittleFord™ Model FM-130-D). The granulator consisted of a cylindrical chamber with capacity of 20 kg, upper and lower sealed doors, a main shaft with four paddles (two V-shaped in the center and two near the sidewalls to prevent dead volume), and two motors. One motor moves the main shaft and the other drives a cutting chopper, which maintains granule size in wet granulations. It also had a spray nozzle for the addition of water or any liquid solution.

After granulation, the mixtures were placed on a motorized sieve tray assembly. The sieve trays for particle size distribution consisted of Tyler's 12 to 70 mesh US Standard testing sieves 20.32 cm of diameter. The sieving was made using a motor shaker (Tyler® RX-24).

The drying phase of the granulations was done on a bench-scale fluidized-bed dryer (Aeromatic AG™ model STREA-1). Its components include a fan, an electrical heater, and other electrical components all mounted in a solid chassis. The granulations were placed in a near conical stainless steel vessel of 0.017 m^3 (16.5 L) capacity with three ports for NIR fiber optic probe mounting as illustrated in Fig. 8. The fan operated with airflows from 40 to approximately 115 m^3/hr and operating temperatures up to 373.15 K (100ºC). Type J thermocouples with insulated wires were installed in the dryer at the entrance and exit of the air. Additional accessories used were a 200 wire mesh to hold the product in place, an air distributor plate with bypass tube, and exhaust air filters (Nylon T695). Also, the fluidized-bed dryer was instrumented with additional control accessories that are tabulated in Appendix C. The process monitoring system used a Windows-based program, running in a personal computer (PC).

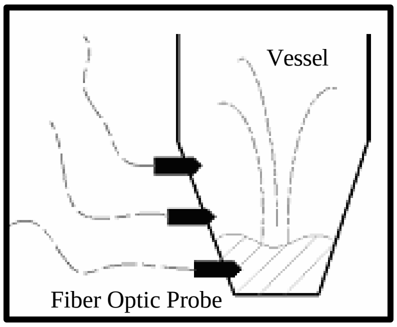

Figure 8. Schematic of fiber optic probe mounting in the fluidized-bed dryer vessel

3.2 Near-Infrared Instrumentation and Calibration

Full NIR spectra were measured using a Fourier Transform (FT)-NIR spectrometer (Bruker Optics™ model Vector 22/N) with a fiber optic probe, Fig. 9. This spectrometer uses HeNe-laser light, a 429 InGaAs diode detector, a quartz beamsplitter and a frequency range of 5,300 to 12,500 cm^{-1}. The probe tip is a flat surface with an area of 78.5 mm^2 or an equivalent diameter of 1 cm.

NIR spectra were obtained with a nominal resolution of 16 cm^{-1} with 32 scans per sampling. The working spectral region is 4196.6 and 9002.7 cm^{-1}, and consisted of 500 data points. A ceramic reference was taken before each set of samples. The collection and

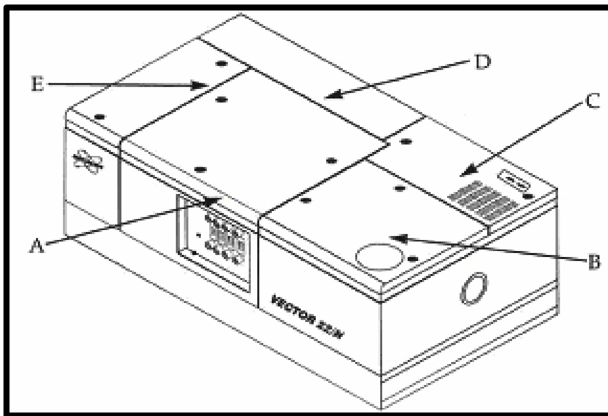

	Name
A	Fiber Optic Compartment
B	Interferometer Compartment
C	Source/ Electronics Compartment
D	Power Supply Compartment
E	Detector Electronics Compartment

Figure 9. FT-NIR (Vector 22/N) spectrometer external view

transformation of spectral data were performed using spectroscopic analysis software. Data acquisition was made through a communication cable connected to an acquisition processor board (AQP), already installed in a second personal computer (PC).

The residual moisture content of granule samples was determined by means of a Karl Fisher (KF) Titration (Methrom™ model 784). First, the equilibration of the Hydranal®-Composite 5 reagent was done using a mixture of 20 cm^3 methanol anhydrous with 10 cm^3 of formamide at ambient temperature. The mixture was intended for use and dissolution of the lactose components in the pharmaceutical formulation, Table 2. Approximately 0.1 to 0.2 g of granules samples were dissolved in the conditioned methanol/formamide mixture, and then it was stirred magnetically for 3 minutes at ambient temperature to ensure complete dissolution of the components before titration. The analysis was done in triplicate and its average was taken as the constituent value of moisture for the sample.

For quantitative analysis of moisture content of powders inside the dryer, NIR spectroscopy needed a multivariate calibration model. The calibration procedure involved collecting a number of samples, obtaining both reference and NIR data on each sample and developing a calibration model from these data by using chemometrics. The reference method for moisture content was the KF method discussed above. The calibration model developed was used to predict moisture in future samples. Internal factors like particle size, sample composition, temperature and homogeneity of samples were covered during the calibration phase.

Four granulation batches were used to withdraw samples at 3-5 minute intervals with different moistures. Due to the large particle size distribution and temperature effects on NIR measurements, granulation batches were only chosen from 20-45 mesh size (~ 0.4-0.8 mm). They were placed in the dryer with an inlet fluidized air temperature of 343.15 K (70ºC) and 80 m^3/hr of airflow. At each time interval, the process was stopped and three samples were withdrawn from different points inside the dryer. Immediately after extraction, six NIR spectra were recorded at different angles on each sample. At the same time, their moisture value was determined with KF titration. The average of these six spectra per sample was entered in the spectroscopic analysis software as the spectral data-set for the constituent moisture value determined by KF. The drying process was re-initialized for another 3-5 minute interval and the procedure was repeated for three more intervals. In general, twelve sample moistures and NIR spectral data-set (absorbances) were obtained from each of the four different batches. This made a total of 48 calibration samples.

The 48 sample moistures and their respective NIR spectral data-set were then used to develop the mathematical expression that relates these two parameters, known as the calibration model. Partial least square (PLS) was used as the calibration tool, in conjunction with spectral pre-treatments, such as first and second derivatives. Validation of the model was performed by applying it to a set of validation samples to test the model's predictive ability. These predicted values were statistically compared to KF reference moisture values measured for the same samples.

3.3 Automation and Control Instrumentation Set-up

Once the NIR calibration was performed, the NIR calibration model was integrated as a part of drying automation used for moisture monitoring. In-line measurements for a real-time drying process were accomplished by using two Windows-based automation and control softwares. The softwares were installed on different PC's and they communicated through a CIO-DAC02 12-bit analog output board. The integration of the apparatus in the automation of the FBD is represented in Fig. 10.

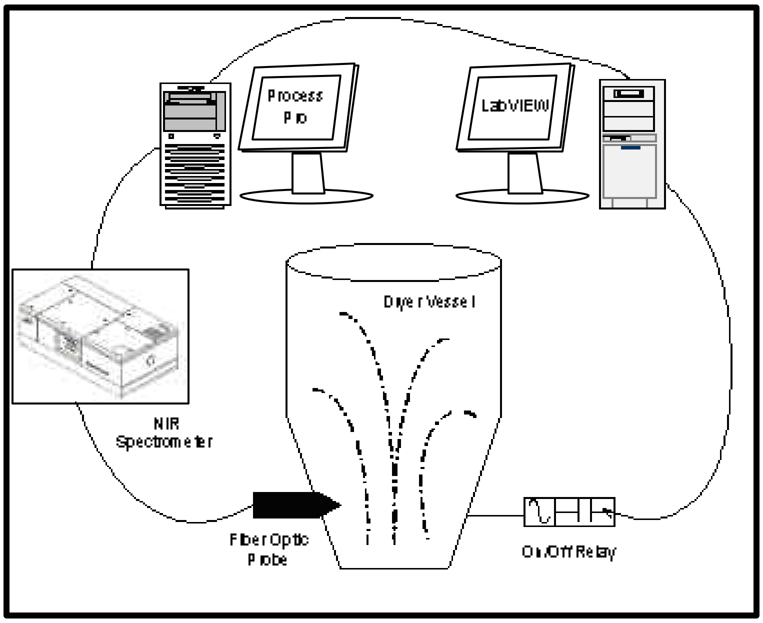

Figure 10. Schematic of the NIR integration in the FBD automation

The control program worked in conjunction with the spectroscopic software to provide an easy-to-use interface for real-time data acquisition and analysis using NIR spectrometers. Analytical results were displayed, logged, and communicated to a remote computer via the analog output board port as a 4-20 mA signal representing the predicted moisture percentage.

Moreover, LabVIEW® software, a graphical programming language that has been adopted for data acquisition and instrument control, received the analog signal results. This information was entered and executed by the control block diagram already built in the LabVIEW® program called virtual instrument (VI). The VI was intended for acquiring the value received via the 4-20 mA signals and to compare it with a set-point value of moisture. Once the drying process had reached the desired moisture value, the LabVIEW® program or VI indicates the on/off switch relay to stop. This communication was done via a data acquisition board (DAQ) installed in the second PC to the relay.

3.4 Mathematical Correlation and Optimization of NIR Measurements

The final objective of the study was to find which external factors can affect, during a FBD drying process, the NIR measurements and thus its moisture predictions. Three heights for probe positioning in conjunction with two levels of bulk mass inside the dryer (0.5, and 1.0 kg), and three fluidization air flows (70, 100, and 115 m^3/hr) were studied. Figure 11 depicts the experimental design used. This was a mixed-level factorial design with 18 treatment combinations with one replicate. Constant variables were temperature of air (same as in the calibration step), powder formulation, Table 2, and initial moisture content (approx. 12.5% w/w water), as well as the particle size distribution (20-45 mesh size).

The air flows were selected based on the diameter ratio, d_r (Wu and Baeyens, 1998). The smaller particle size used was 0.4 mm and the larger size was about 0.8 mm giving a d_r of approximately 2. The minimum fluidization air flow determined by test trials was 40 m^3/hr (~ 0.2 m/s). According to the studies of Wu and Baeyens, an air flow of 70 m^3/hr (~ 0.4 m/s) or more must be sufficient to presume a good mixing of particulates while flowing and a minimum effect of segregation.

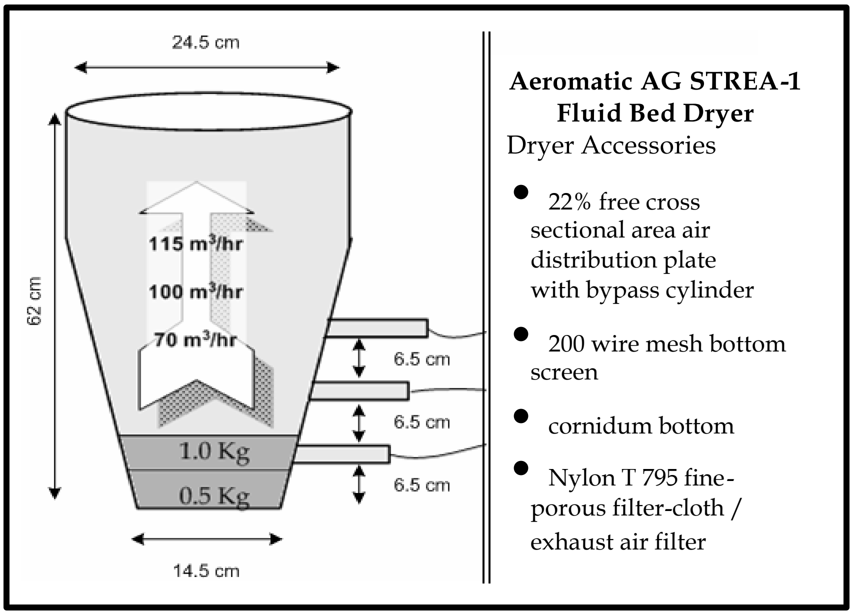

Figure 11. FBD and experimental design schematic

Spectra were recorded from each set of experiments (height, bulk mass and air flow) approximately after 10 minutes of drying without stopping the process. Each spectrum was used to predict the moisture content of the powder at that time using the NIR calibration model developed previously. Immediately after taking the spectra, the process was stopped to withdraw one sample from the vessel and to analyze it with the NIR spectrometer and with the KF titration to monitor the equilibrium moisture.

The response variable was based on the difference between the NIR moisture predicted in-line versus the NIR value predicted statically. Mathematical and statistical analysis was applied to determine which factors were significant for the prediction error. A statistical equation was developed in which one can maximize the NIR performance (minimize the prediction error) as a function of probe positioning, fluidization air-flow and bulk mass inside the dryer. Therefore, an empirical correlation was established for the prediction of the optimum probe position that minimizes the errors in the NIR measurement given a set of conditions such as the initial bulk mass and fluidization velocity.

CHAPTER IV: RESULTS AND DISCUSSION

4.1 NIR Calibration Model for Moisture Prediction

The first step in the development of an automated FBD process using the NIR technology was to build-up a proper calibration model. Table 3 summarizes the data obtained using four different batches of granulations made with the excipients and proportions already discussed on Chap. 3.

Figure 12 depicts the expected behavior for a formulation that is almost 86% lactose (Popó et al., 2002). This image presents the variation in absorbances due to moisture differences between samples. A noticeable band near 5176 cm^{-1} (~ 1490 nm) is observed, which is characteristic of the O-H vibrations recognized in the literature (Choppin and Buijs, 1963, Osborne et al., 1993). There was an increase in NIR absorption with an increase in water content.

The NIR spectra presented on Fig. 12 in conjunction with its constituent moisture value were analyzed using the spectroscopic software. The chemometric algorithm applied was partial least squares (PLS). Four criteria values were used to determine the optimal calibration model: the correlation coefficient (R^2), the root mean square error of estimation (*RMSEE*), the root mean square error of cross validation (*RMSECV*), and the root mean squared error of prediction (*RMSEP*). These criterion values are presented in the tables and figures below to illustrate the development of the calibration model.

The cross-validation process was automatically done by the software in which the program leaves one standard out of the regression and tests it using the remaining data. The *RMSEP* was used when test-set spectra not used to build the regression were

Table 3. Data of Sample's Moisture Content for NIR Calibration Model

	Sample name*	**Moisture %** **(determined by KF Titration)**
Calibration Lot #1	1.0.a	13.21
	1.0.b	13.42
	1.0.c	12.97
	1.5.a	10.05
	1.5.b	9.79
	1.5.c	10.44
	1.15.a	5.41
	1.15.b	5.35
	1.15.c	5.72
	1.25.a	5.09
	1.25.b	5.15
	1.25.c	5.03
Calibration Lot #2	2.0.a	13.59
	2.0.b	13.75
	2.0.c	14.13
	2.7.a	10.17
	2.7.b	10.13
	2.7.c	10.30
	2.14.a	5.88
	2.14.b	6.26
	2.14.c	6.06
	2.21.a	5.48
	2.21.b	5.55
	2.21.c	5.38
Calibration Lot #3	3.0.a	13.54
	3.0.b	12.85
	3.0.c	12.80
	3.3.a	10.61
	3.3.b	10.56
	3.3.c	10.46
	3.8.a	7.36
	3.8.b	6.74
	3.8.c	6.65
	3.13.a	5.26
	3.13.b	6.32
	3.13.c	5.90
Calibration Lot #4	4.0.a	13.40
	4.0.b	13.10
	4.0.c	13.15
	4.5.a	7.32
	4.5.b	8.21
	4.5.c	7.35
	4.10.a	5.79
	4.10.b	5.78
	4.10.c	5.77
	4.20.a	6.63
	4.20.b	5.61
	4.20.c	5.71
Test-set Lot #5	5.0.a	13.12
	5.4.a	8.29
	5.8.a	6.00
	5.16.a	5.40

* The sample names are coded with the following sequence: the first number indicates the lot number, the second number indicates the drying time elapsed when the sample was taken, and the letter indicates that three samples were withdraw at this same time. The shaded line indicates an outlier.

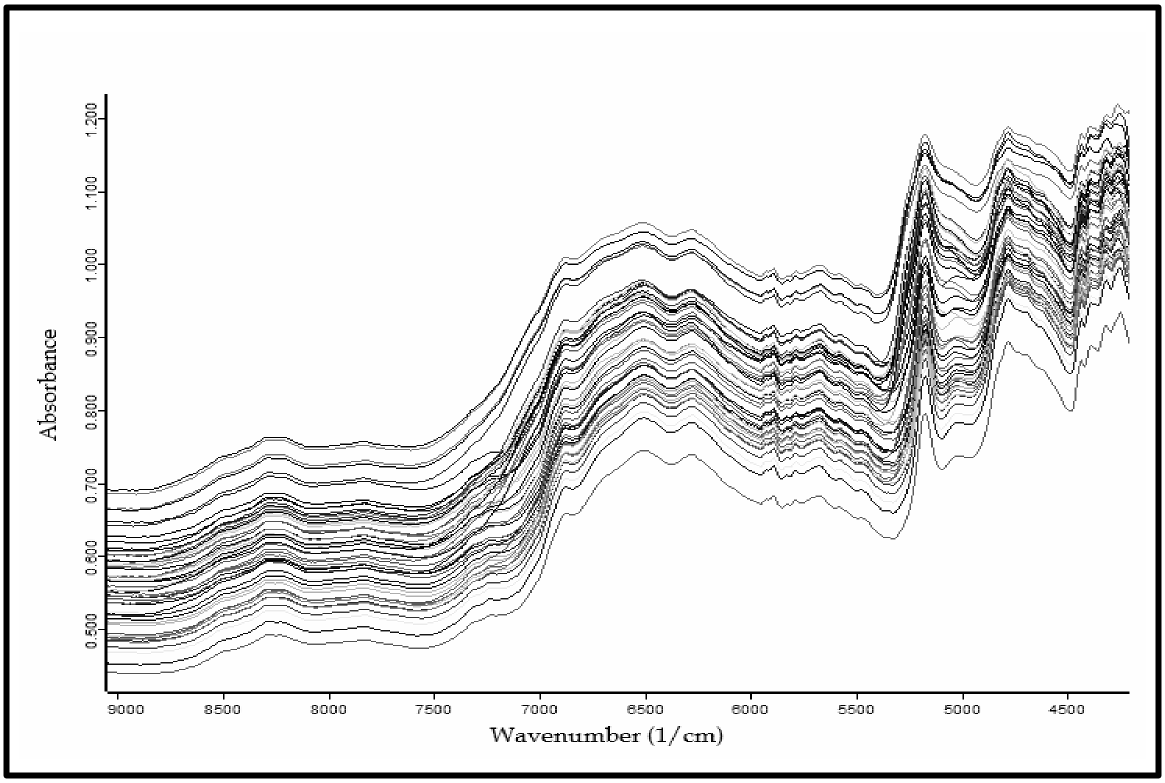

Figure 12. NIR absorbance spectra for moisture calibration model

predicted to challenge the NIR model. All the root mean squares values were expected to give the minimum possible number in order to accomplish the best fitting.

Several pre-treatments were executed to ensure a regressional fitting that could predict future samples with minimal error. A summary of the different criteria values obtained using some pre-treatments in the calibration model are provided on Table 4. Noticed that the *RMSEE* and *RMSECV* were related to the self-testing and cross-validation of the model using the same 48 standard samples listed on Table 3. On the other hand, *RMSEP* was directly related to test-set samples, and moreover, to future unknown samples.

Table 4 compares the different R^2 values obtained with some of the most used pre-treatments in the literature. Vector normalization has the best fitting for validation

Table 4. Comparison of Pre-Treatments Effects in the NIR Calibration Model

Pre-Treatment Type	**Optimum Rank**	**R^2 (for cross-validation)**	**RMSECV**	**R^2 (for self-testing)**	**RMSEE**	**Test-Set Prediction Residual Average***
No Pre-treatment	5	97.63	0.49	98.43	0.43	0.21
Min-max normalization	4	98.24	0.42	98.96	0.34	0.44
Vector normalization	4	98.44	0.40	98.90	0.35	0.33
First derivative	4	97.98	0.46	98.74	0.38	0.32
MSC	4	98.38	0.41	98.87	0.36	0.35

*Test-set spectra values are shown on Fig. 14. These spectra were evaluated using regression models executed with the pre-treatments listed on this table. The difference between the true and the fitted NIR values were evaluated and the average of the four samples was taken as the residual average for each pre-treatment.

and calibration but, unfortunately, its correlation did not have the best prediction in the test-set samples. The difference in the correlation coefficient for these pre-treatments was minimum compared to no-pretreatment at all. Thus, the final decision was primarily based on the test-set residual average. In this case, the application of PLS with no spectral pre-treatment seems to predict test-set samples with higher precision.

The final calibration model included 47 of the 48 data points listed on Table 3. Experiment 4.20.a was classified as an outlier giving a calibration correlation coefficient of 98.43 compared to the 98.68 of the coefficient calculated without the outlier. Even though the difference was minimal, this improvement in the coefficient produced better predictions in the test-set samples. Figure 13 shows the graphs of NIR prediction versus true moisture values with and without outliers. These graphs reached 45° angles as the model approached better fitting. The circled point is the outlier.

The test-set spectra consisted of four different samples that were not used to perform the regression, Table 3. The samples were taken and analyzed in the same way as all the samples used for calibration. As discussed above, a simple change in the regression coefficient produced a small improvement in the NIR prediction of the test-set spectra. As can be seen from Fig. 14, the exclusion of the outlier value from the PLS regression model had caused a better fit on future unknown samples.

The chemometric software determined the best rank value for the regression automatically. For both model regressions (with and without outlier), a rank of 5 was determined as the optimum number of factors that can fit or predict moisture values with minimal error. The addition of more factors does not contribute significantly to the

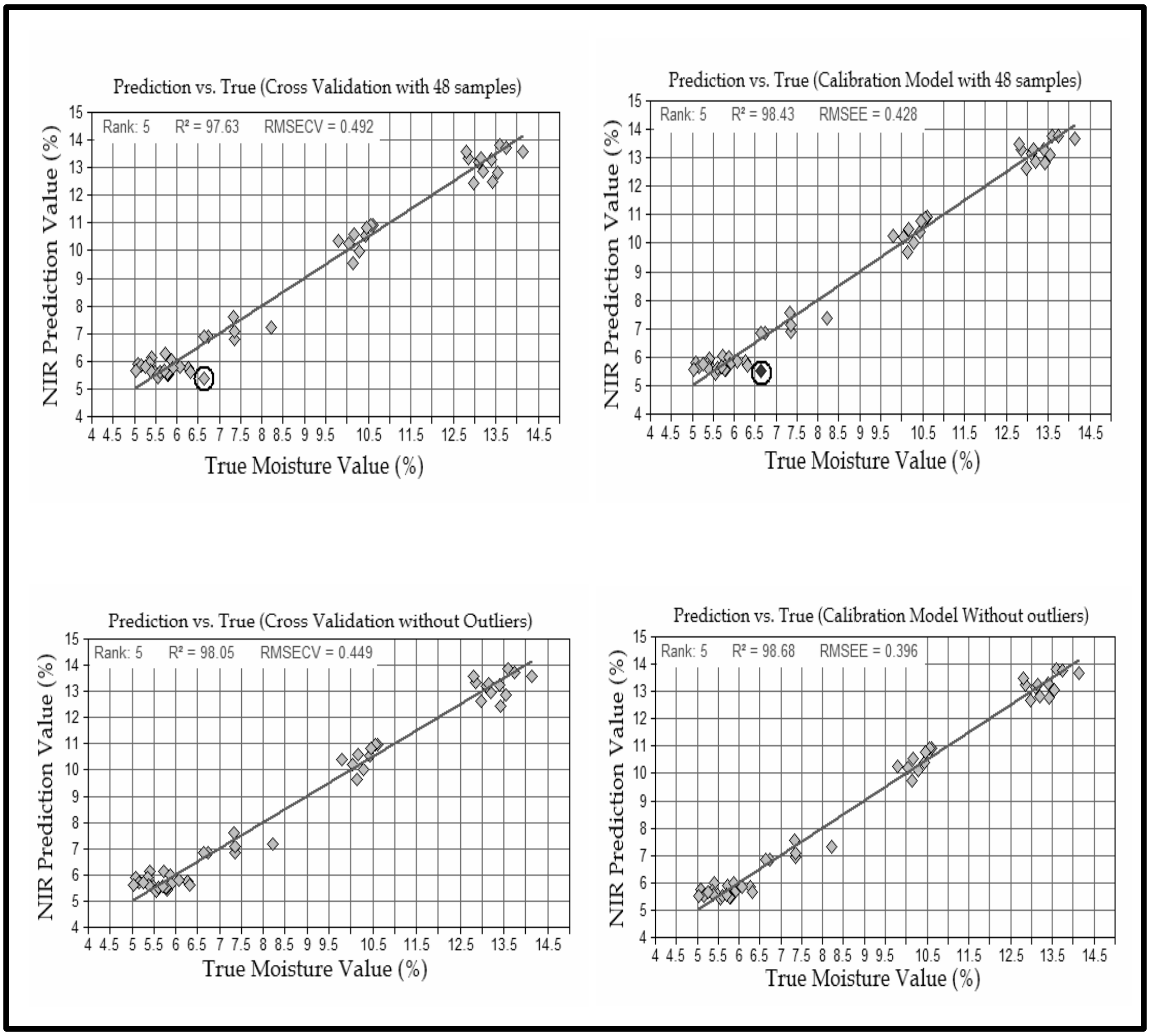

Figure 13. NIR prediction vs. true value of moisture content

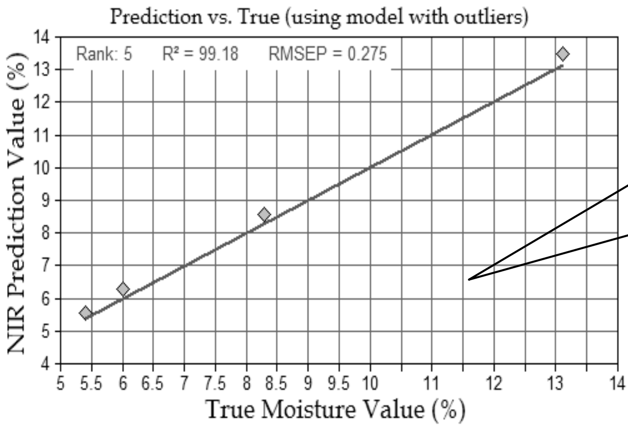

Sample Name	True Moisture Value (%)	NIR Model Value (%)	Residual
5.0.a	13.12	13.49	0.37
5.4.a	8.29	8.56	0.27
5.8.a	6.00	6.27	0.27
5.16.a	5.40	5.55	0.15

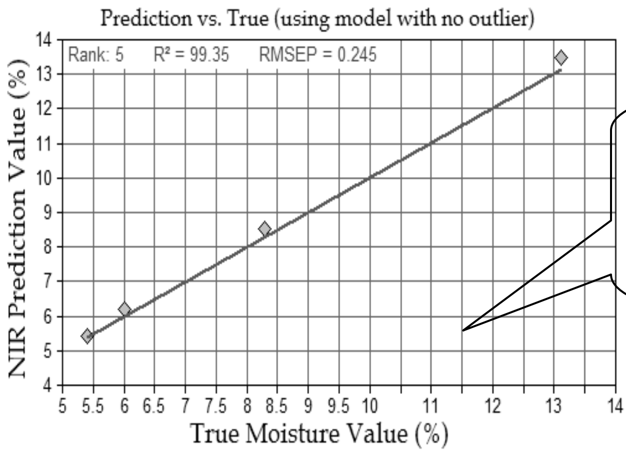

Sample Name	True Moisture Value (%)	NIR Model Value (%)	Residual
5.0.a	13.12	13.49	0.37
5.4.a	8.29	8.54	0.25
5.8.a	6.00	6.20	0.20
5.16.a	5.40	5.42	0.02

Figure 14. Comparison of NIR prediction vs. true value for test-set spectra

improvement of the predicted NIR values. The addition of unnecessary factors could affect negatively future unknown samples (Siesler et al., 2002, Wetzel, 1983).

Table 5 shows the calculated regression coefficients and root mean squares for the cross-validation and self-testing process done on the final regression model without outliers. Slight favorable changes can be seen on the self-testing process but not on the cross-validation for ranks higher than 5. In cases like this, the cross-validation has more weight on the final selection of the rank because this process involves to "leave-one-out" and test with the remaining data. Practically, each standard is considered as a test-set spectrum.

Table 5. Rank's Effect on the Statistical of the Final Regression Model with No Outliers

Rank	R^2 (for cross-validation)	RMSECV	R^2 (for model self-testing)	RMSEE
1	60.92	2.01	63.55	1.99
2	88.84	1.08	90.44	1.03
3	97.86	0.47	98.23	0.45
4	97.80	0.48	98.54	0.41
5	98.05	0.45	98.68	0.40
6	98.15	0.44	98.77	0.39
7	98.06	0.45	98.87	0.38
8	97.80	0.48	99.32	0.30
9	98.25	0.43	99.45	0.27
10	98.04	0.45	99.54	0.25

4.2 Factors Analysis and NIR Optimization Results

Figure 15 shows the differences between spectra taken at-line and in-line while varying the experimental conditions. NIR spectra taken from axial probe position #3 were concentrated at the top of the graph showing high baseline shifts, especially those taken at lower air flows. The absence of defined bands demonstrated that there was no representative amount of sample reaching the NIR probe tip, and the resulted absorbances were mostly noised signals.

At-line and axial position #2 spectra concentrated mostly at the middle of the graph. In this situation, the observed bands and absorbances permit a satisfactory NIR moisture prediction for almost all the operating conditions used. Most of the NIR predictions at that position were similar to the static samples. Thus, it can be considered that the NIR prediction in axial position #2 is almost independent of the operating conditions used in this experiment.

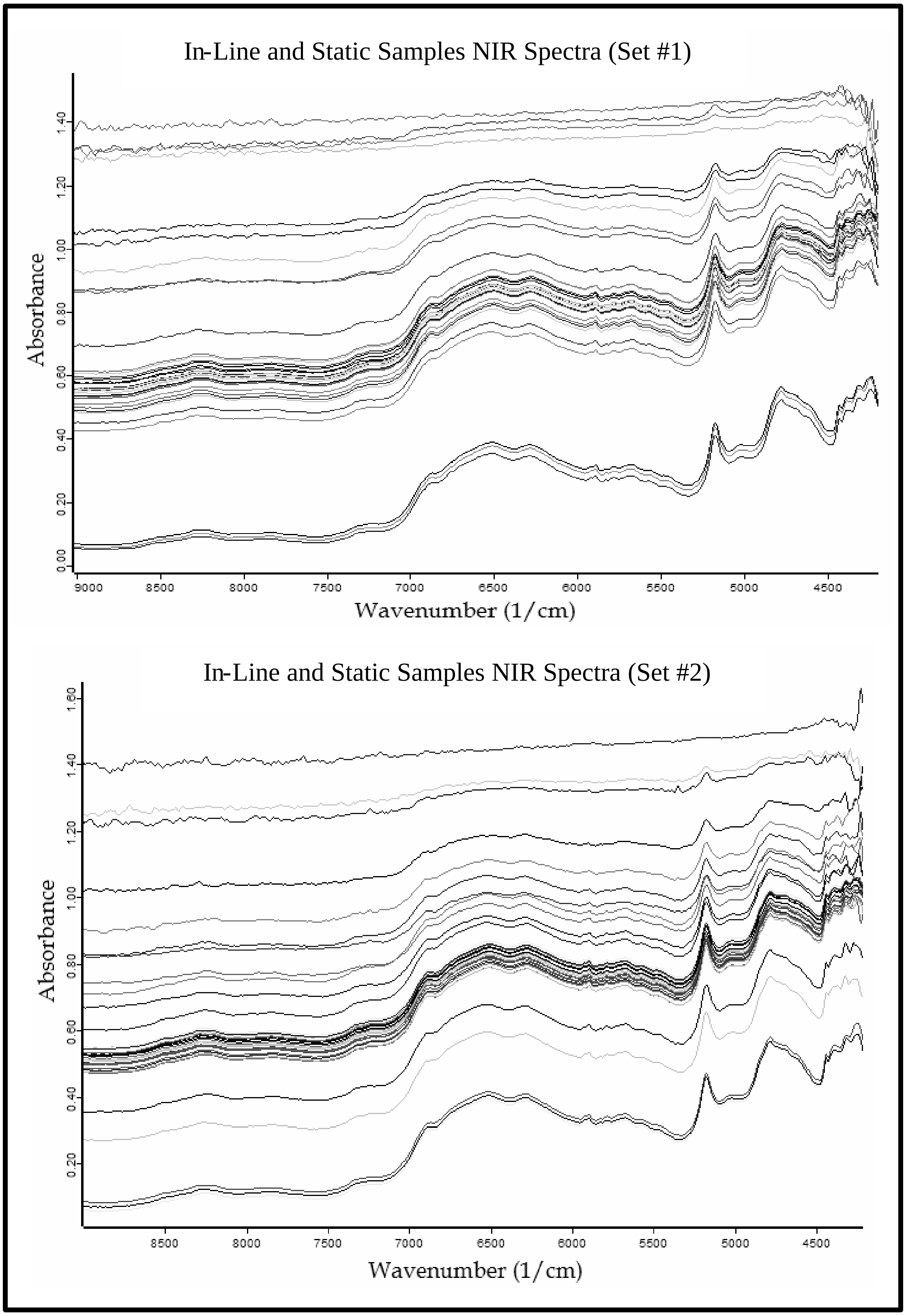

Figure 15. In-line and static samples NIR spectra for both experiment sets

NIR bands observed using axial position #1 had lower baselines than static samples. Similar results were encountered by Andersson et al. (2000). They found that spectra collected while running the coating process were observed to have baseline levels irregularly spaced caused by differences in the packing of pellets, or by differences in particle size within the batch.

Figures 16 to 18 depict the interaction effects of bulk mass and probe axial position on the residual (static minus in-line NIR moisture prediction). These graphs illustrate that air flow has opposite effect on axial positions 1 and 3. The prediction residual increased with air-flow for axial position #1, while decreased for axial

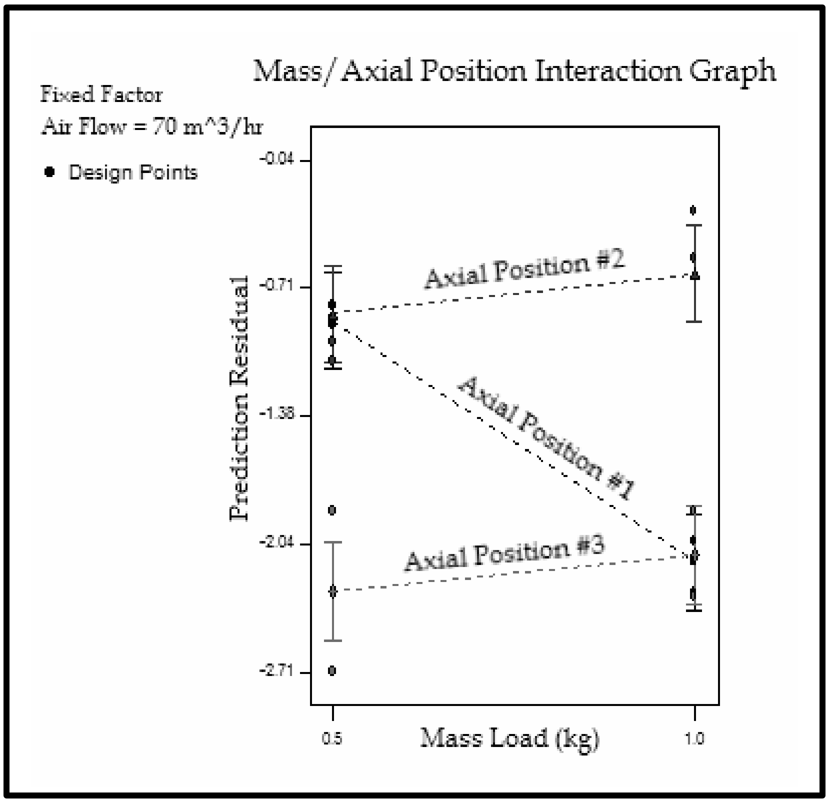

Figure 16. Mass vs. axial position interaction effect for the lowest level of airflow

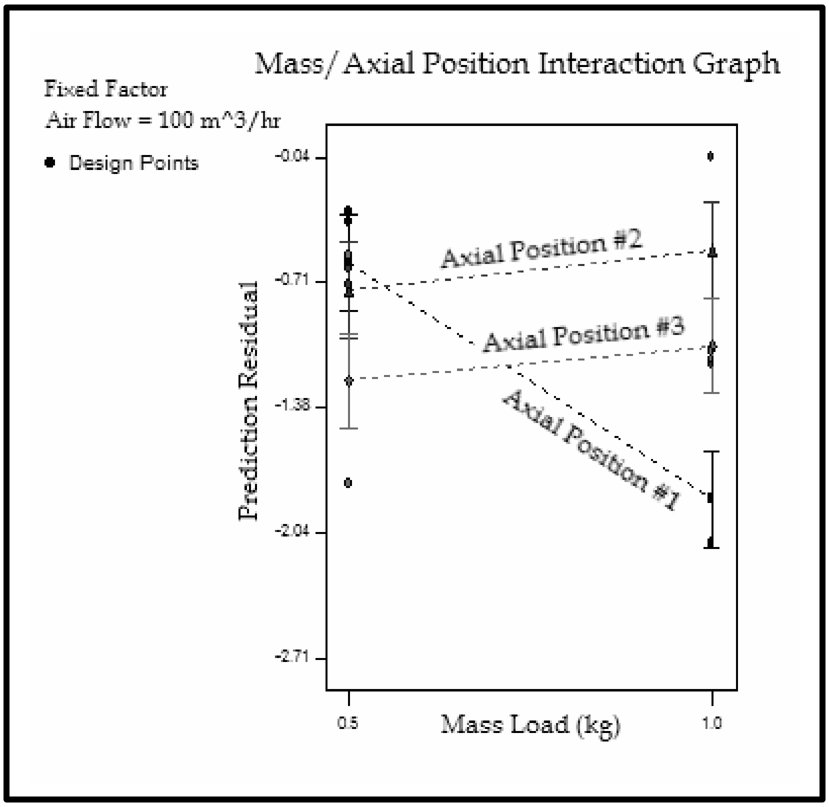

Figure 17. Mass vs. axial position interaction effect for the medium level of airflow

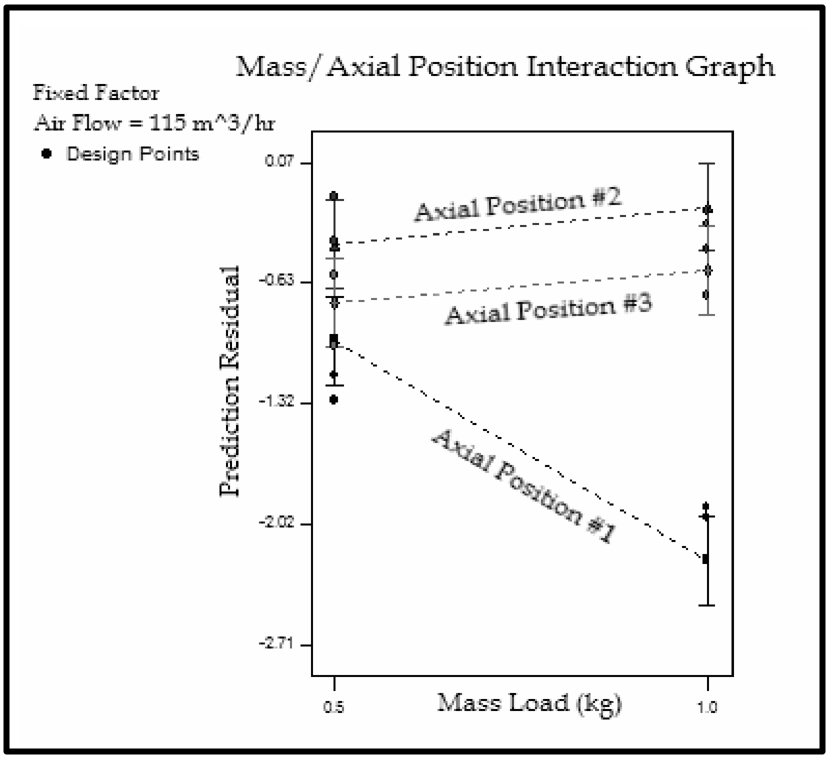

Figure 18. Mass vs. axial position interaction effect for the highest level of airflow

position #3. A similar behavior is also encountered with variations of the bulk mass. On the other hand, the residuals for axial position #2 had no significant variations with any of the factors. NIR measurements using this position provided residuals less than one. Statistically, axial position #2 was the best choice for in-line measurements.

The behavior observed in NIR prediction while varying the operating conditions could be due to the particle size distribution and the sample density distribution inside the dryer vessel. Even though particle size variation was carefully limited for the experimentation, the fluidization might promote apportion inside the vessel. Additional NIR testings were performed on two different static samples of a sieved batch. Figure 19 revealed that there were no appreciable differences between spectra of samples of different particle size. This can be expected in lieu that the particle variations used in the batches were small. According to the work of Wu and Baeyens (1998), the air flows used in the experimentation should prevent the segregation of the fluidizing particles by promoting a good mixing along the bed.

The small absorbance offset in Fig. 19 is in agreement with that discussed by MacDonald and Prebble (1993), which they attributed to the particle size differences. The absorbance increase as particle size increase (see Eqs. 2 and 3). The NIR model predictions for both particle sizes were similar and their residuals were small indicating that the slight difference in the absorbance did not affect significantly the NIR prediction. Therefore, particle size distribution was not the specific responsible of the NIR prediction errors.

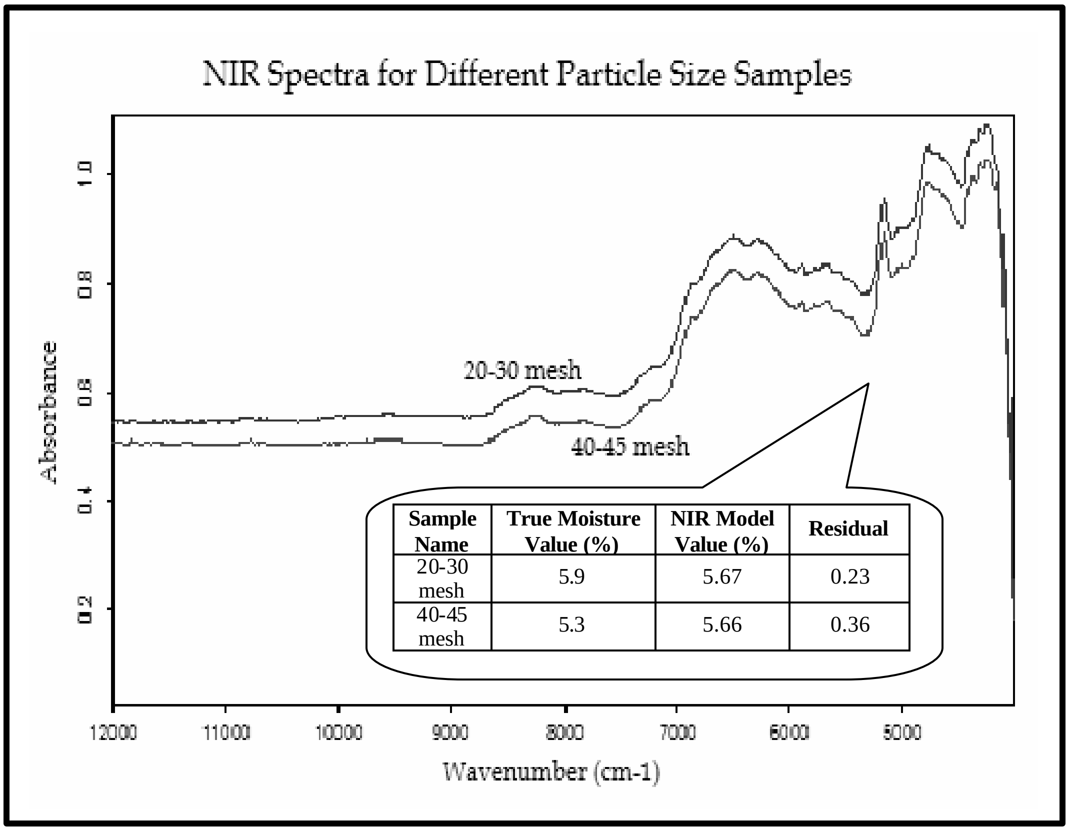

Figure 19. NIR spectra for 20-30 and 40-45 mesh size samples

Sample density distribution along the bed is the more probable explanation for the behavior encountered with the residuals variations for the in-line NIR predictions. Sample presentation or how to present a sample to a NIR instrument is one of the important factors affecting NIR measurements (Siesler et al., 2002). The cells used for powder samples had to ensure constant and reproducible packing density; because packing density affects scattering conditions.

According to Popó and collaborators (2002), NIR irradiation in a mixture of ibuprofen and lactose could reach a depth up to 2 mm. The crystal cells used for static NIR measurements in the calibration phase had approximately 4 mm of diameter. Packing density distorts the depth of penetration and orientation of interfaces between light and sample (Pasikatan et al., 2001). Fluidization inside the dryer vessel has to ensure an analogous distribution and packing to maintain the same conditions as those used in the calibration phase.

The three spectra on Fig. 20 revealed noticeable variations for in-line spectra taken at different axial positions. In this figure was appreciated, that for a fixed air-flow and mass load, the absorbance and appearance of the spectra changed significantly with respect to the axial probe position.

High baselines and poor defined bands in axial position #3 are a representation of low sample density at that point (Siesler et al., 2002). As sample density decreases, radiation penetrates deeper into the powder, Fig. 2. The increase in the path length that the light travels decreases the scattering coefficient as shown on Eq. 3, thus reducing the diffuse reflection. The emitted light was highly dispersed probably by turbulent air flow

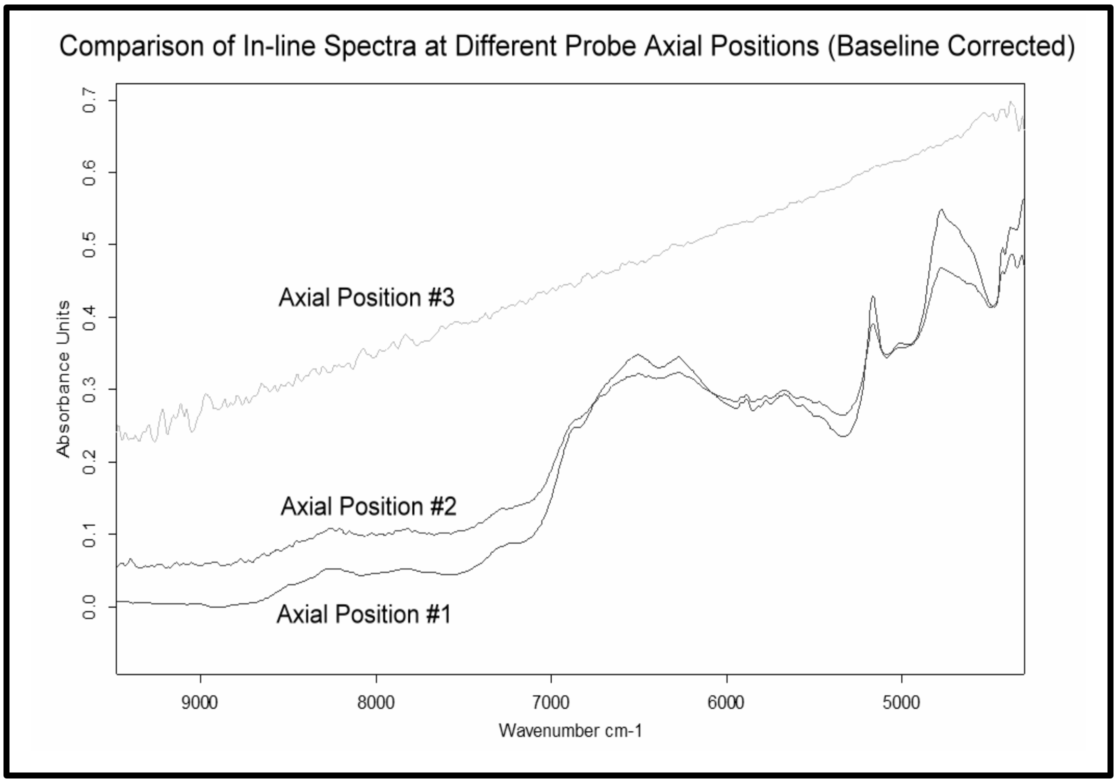

Figure 20. In-line NIR spectra for a fixed air flow of 70 m^3/hr and a mass load of 1.0 kg

conditions (Mujumdar, 1987) on that zone and no substantial quantity of light can be reflected back to the detector.

On the other hand, axial position #1 showed much defined bands but a slight lower absorbance; a possible indication of differences in packing density in that zone. Randomness in the orientation of the interfaces and amount of material are essential to bring complete diffusion of light (Wetzel, 1983). Compaction and agglomeration of the particles might destroy complete randomness causing a decrease in the path length that the light travels. Therefore, the scattering coefficient increases and more light are reflected back to the detector (Pasikatan et al., 2001).

4.3 ANOVA Results and Regressional Fitting

The next step was to demonstrate the feasibility of using NIR spectroscopy for the FBD automation by showing the ability of predicting effectively in-line samples without stopping or disturbing the drying process.

In order to diminish discrepancies on in-line measurements and to guarantee minimal NIR testing errors, an experimental design was developed. The final inputs for the experimental design are in Table 6. The raw experimental data is in Table 18 on Appendix B. A total of 36 experiments were divided into two sets; making one full set and a replicate. The two sets were separated into blocks because each set was done using different granulation lots. The experiments were run with no particular order or sequence to fulfill the characteristics of a completely randomized experimental design.

The fifth column on Table 6 is an average of static NIR values. The first nine experiments belong to a mass load of 0.5 kg. All these samples were taken using the same

Table 6. Prediction Residual Data for Experimental Design Analysis

	Air Flow (m^3/hr) (B)								
	70			100			115		
Mass (kg) (A)	Axial Position 1 (C)	Axial Position 2	Axial Position 3	Axial Position 1	Axial Position 2	Axial Position 3	Axial Position 1	Axial Position 2	Axial Position 3
0.5	-0.80 -0.90	-1.09 -0.99	-2.71 -1.87	-0.39 -0.33	-0.64 -0.72	-1.78 -0.57	-1.30 -1.16	-0.39 -0.13	-0.99 -0.59
1.0	-2.29 -2.03	-0.55 -0.31	-2.32 -1.87	-2.10 -2.11	-1.15 -0.04	-1.12 -1.08	-1.92 -1.98	-0.43 -0.22	-0.70 -0.29

mass batch in the dryer. The same applies to the following sets of nine experiments. The static samples from each set were taken from the same batch already dried to approximately 5-6% moisture. This reduces the NIR prediction errors on the static sample testing due to a slight variability on the moisture content at different points in the dryer.

The information shown on Table 6 was entered in the statistical experimental design software. Appendix B presents a table with the equations to perform the analysis of variance of this study.

The ANOVA for the full mixed-level factorial design indicated that the mass load, air-flow and axial position affected the in-line NIR prediction; with an *F* Probability distribution of 0.05. Small *F* Probability values (less than 0.05) in the individual model terms have a significant effect on the response. The complete software output is presented on Appendix B. In Table 7 is observed the final ANOVA results excluding the non-significant terms; the remaining terms were used to develop a predictive model.

Appendix B presents also the full software output for Table 7 in which a predictive model was calculated using the significant terms resulted from the factorial

Table 7. ANOVA Summary for the Mixed-Level Factorial Design

Source	Sum of Squares	Degrees of Freedom	Mean Square	F value	Prob > F
Block	0.83	1	0.83		
Model	16.29	11	1.48	16.35	<0.0001
Mass Load (A)	0.74	1	0.74	8.17	0.0089
Air Flow (B)	2.62	2	1.31	14.48	<0.0001
Axial Position (C)	5.57	2	2.79	30.77	<0.0001
AC	4.25	2	2.12	23.46	<0.0001
BC	3.10	4	0.78	8.57	0.0002
Error	2.08	23	0.091		
Total	19.20	35			

analysis. The final equation was in terms of coded factors (see Table 9):

$$\begin{aligned} \Pr ed\ \operatorname{Re} s = & -1.11 - 0.14A - 0.37B_1 + 0.10B_2 - 0.34C_1 + 0.55C_2 - 0.49AC_1 \\ & + 0.25AC_2 + 0.31B_1C_1 + 0.11B_2C_1 + 0.19B_1C_2 - 0.19B_2C_2 \end{aligned} \tag{11}$$

The predictive model had a coefficient correlation of 0.89, and a standard deviation of 0.30. This R^2 is less than what is usually expected for a regression equation, but it gives an indication that the data can be adjusted to fit a model. Empirical correlations are based and supported with multiple replications of data. Technical and instrumental complications limited the analysis to only two sets of experiments.

The diagnostic checking of this predictive model was supported by comparing the actual values from Table 6 and the values predicted by the model. Figure 21 depicts the normal probability plot of the residuals between actual and predicted values. This graph indicated whether the residuals follow a normal distribution, in which case the points followed a straight line.

Figure 22 is another diagnostic checking based upon a graph of actual residual values from Table 6 and those calculated using the predictive model on Eq. 11. The graph illustrates the difficulties presented by Eq. 11 in adjusting the data on Table 6 to a 45°

Table 8. List of Coded Factors Used in the Predictive Model

Factor	Levels	Coded Symbol
Mass Load	0.50	A = -1
	0.75	A = 0
	1.00	A = 1
Air Flow	70	$B_1 = 1, B_2 = 0$
	85	$B_1 = 0.5, B_2 = 0.5$
	100	$B_1 = 0, B_2 = 1$
	108	$B_1 = -0.5, B_2 = 0$
	115	$B_1 = -1, B_2 = -1$
Axial Position	1	$C_1 = 1, C_2 = 0$
	2	$C_1 = 0, C_2 = 1$
	3	$C_1 = -1, C_2 = -1$

*Shaded lines are levels not used in the experimental design

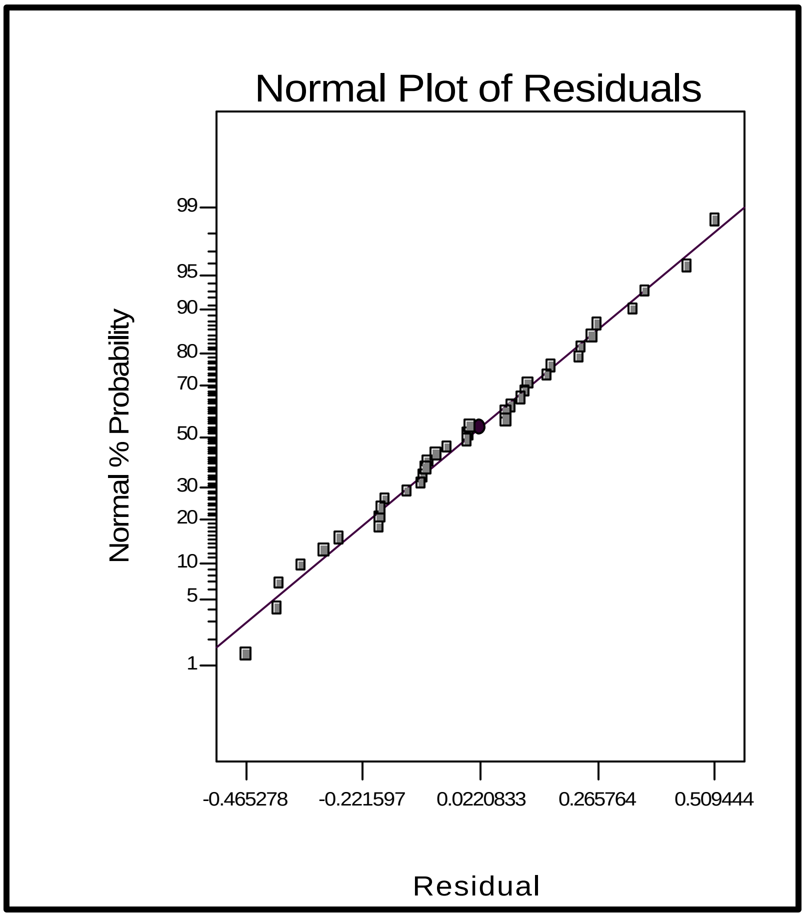

Figure 21. Normal probability plot for the predictive model

degree line.

The actual vs. predicted residual values do not followed a straight 45° degree line, but the model reflects a good performance in trying to fit a regressive model. Presumably, more replications of experiments are needed to get a coefficient correlation higher than 0.89 (Montgomery, 2001).

Additional NIR testings were made to account the validity and usefulness of Eq. 11. In-line NIR prediction residual could be estimated using this equation and the coded factors presented on Table 8. As an example, the NIR prediction residual for a mass load of 0.75 kg, an air flow of 70 m^3/hr, and measured in axial position #1 is:

$$\begin{aligned} Pr\,ed\ Re\,s = & -1.11 - 0.14(0) - 0.37(1) + 0.10(0) - 0.34(1) + 0.55(0) - 0.49(0)(1) \\ & + 0.25(0)(0) + 0.31(1)(1) + 0.11(0)(1) + 0.19(1)(0) - 0.19(0)(0) \end{aligned}$$

$$Pr\,ed\ Re\,s = -1.51$$

This value is not exact, but agreed with the calculated NIR prediction residual for an in-line and a static testing made at the same conditions. Table 9 summarizes the same estimation for other conditions. The estimated residuals are not identical, but Eq. 11 can

Table 9. Summary of NIR Prediction Residuals Using The Predictive Model of The Experimental Design

Factors Levels		**In-line NIR moisture prediction (%)**	**At-line NIR moisture prediction (%)**	**[1]Prediction Residual A**	**[2]Prediction Residual B**	**[3]Difference**
Mass = 0.75 kg Air Flow = 70 m^3/hr	Position 1	7.38	5.52	-1.86	-1.51	-0.71
	Position 2	6.60	5.53	-1.07	-0.74	-0.33
	Position 3	9.80	5.54	-4.26	-2.19	-2.07
Mass = 0.75 kg Axial Position #3	Air flow 70	9.80	5.54	-4.26	-2.19	-2.07
	Air flow 100	6.38	5.41	-0.97	-1.14	0.17
	Air flow 115	6.19	5.53	-0.66	-0.63	-0.03

[1]The residuals here are the difference between the third and the second columns.
[2]The residuals in this column correspond to those calculated using Eq. 11.
[3]These differences are based on the fourth and fifth columns.

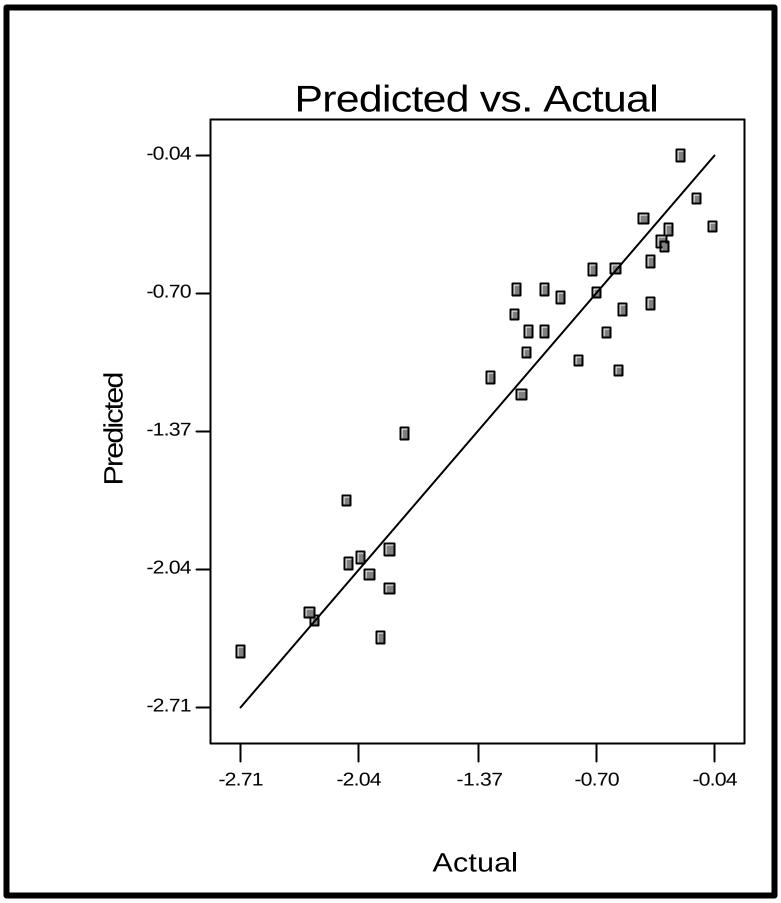

Figure 22. Plot of predicted residuals from Eq. 11 vs. actual residuals values from Table 6

be helpful in figuring out NIR prediction residuals prior to measuring. More experimental sets would help to refine this equation.

4.4 Implementation of Control Algorithm

The programming capabilities of the LabVIEW® graphical language provided sufficient tools to implement a control strategy. Figure 23 illustrates the implementation of the user interface and control algorithm written using this software.

The control strategy could be applied from the start of the drying process, but subtle implications could not guarantee adequate moisture NIR readings. In the first few minutes of the operation, the powders were too moist and this caused particulate agglomeration and stickiness in the tip of the fiber optic probe. Difficulties were contemplated back in the development of drying curves as shown on Fig. 24. These plots compared the moisture values obtained using three different sources in which the in-line NIR moisture predictions deviates significantly from the real KF moisture values at the beginning of the drying curve. Therefore, in-line NIR testings were done at the

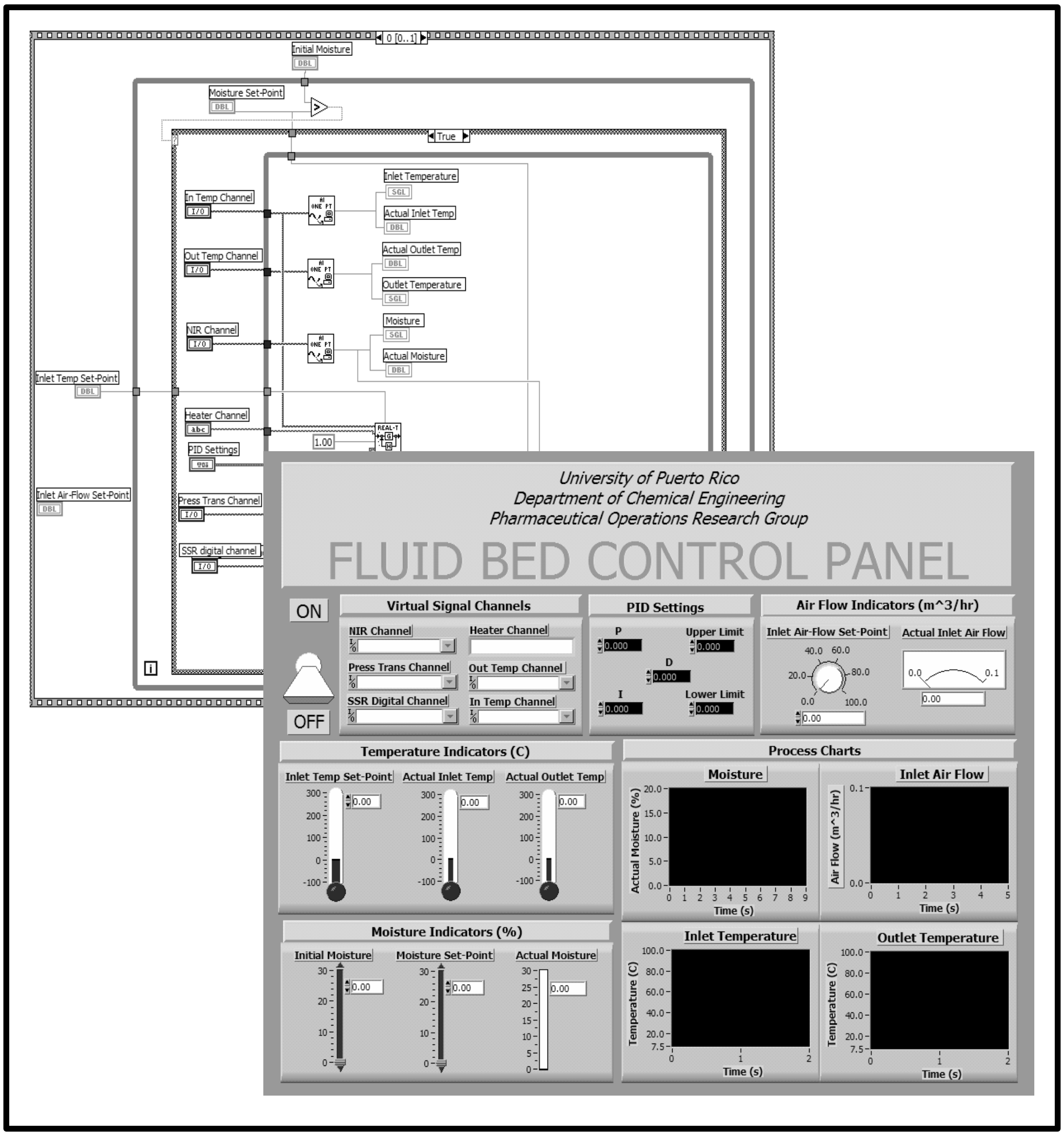

Figure 23. Graphical user interface and algorithm for the control strategy

equilibrium value that was between 5-6 % moisture. Future experimentation of this kind must consider the application of a mechanical or pneumatic artifact to clear the probe up before the acquisition of spectra.

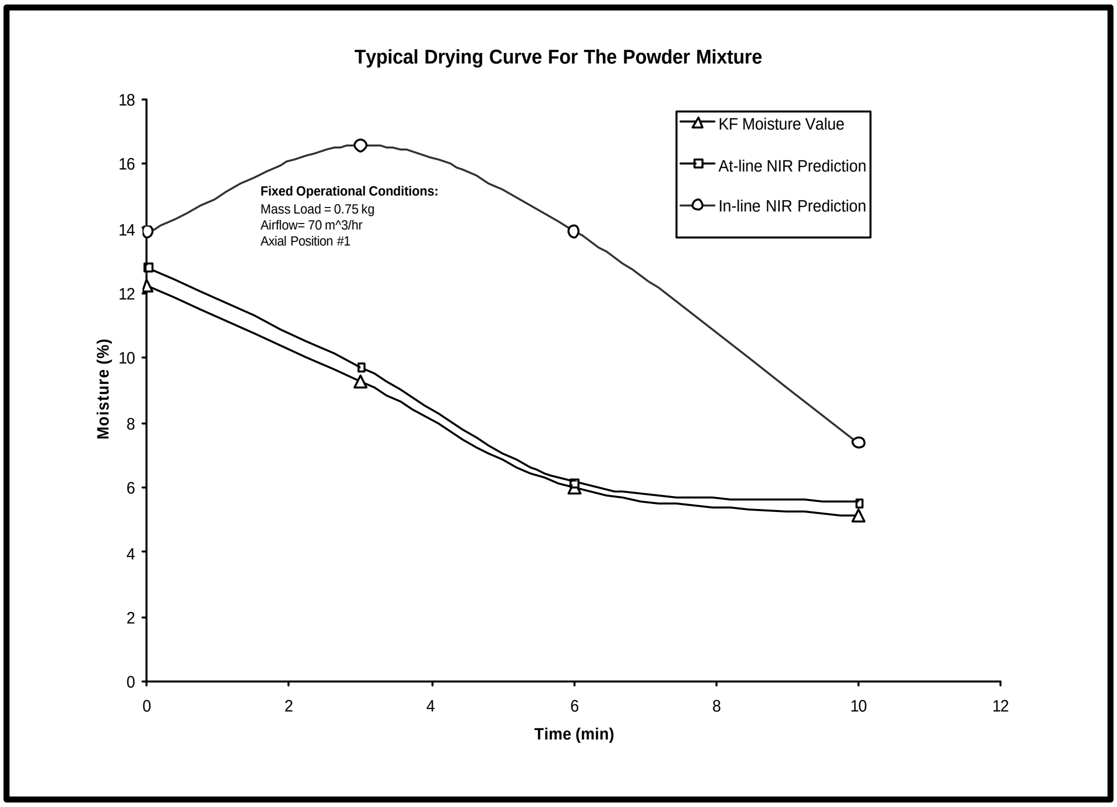

Figure 24. Comparison of drying curves with moisture values from different analytical sources

CHAPTER V: CONCLUSIONS AND RECOMMENDATIONS

The PLS algorithm provided a good calibration model to predict static samples with residuals less than one. There was an increase in NIR absorption with an increase in water content. Several pre-treatment algorithms were applied to improve the model prediction, but none of them contributed significantly to this process, thus no pre-treatments were needed. The calibration model with no pre-treatment predicted at-line samples with more precision than the other models.

The experimental design showed that in-line measurements deviated significantly from static samples depending on the FBD operating conditions. The prediction residual increased with air flow for axial position #1, while decreased for axial position #3. A similar behavior was also encountered with variations of mass load. On the other hand, the residuals for axial position #2 had no significant variations with any of the other factors. NIR measurements using this position provided residuals less than one. Axial position #2 resulted to be the choice for most accurate in-line measurements.

A mathematical correlation was developed to predict residuals as a function of the operating conditions used. This correlation can also be used to find optimal operating conditions that could satisfy suitable prediction residuals. This statistical correlation can predict residuals with an $R^2 = 0.89$ and a standard deviation of 0.30. This correlation took into account only two experimental sets.

Measurements during the first few minutes can not be handled adequately because too much moisture variations were found at this stage. Moreover, the powders with moistures higher than 7% w/w had a tendency to stick to the tip of the fiber optic probe, making it even more difficult to collect spectra from a representative portion of the bulk mass inside the dryer. Future experimentations must consider the application of some device to clean the tip of the probe before analysis.

Recommendations for the implementation of NIR could be the application of two or more fiber optic probes in the dryer vessel to collect spectral data at strategic points. The average of the spectra data collected at the same time may improve the NIR prediction of the average moisture in the powders.

Other applications could be the development of an in-line calibration model by choosing optimal points for NIR measurements according to the results obtained in this experimental design. Now that axial position can be considered the best measuring position for NIR, a calibration model can be designed using in-line testings.

REFERENCES

1. **Aldrich, D.S., and M.A. Smith**. 1999. Pharmaceutical applications of infrared microspectroscopy. *App. Spect. Rev*. **34**(4): 275-327.
2. **Alvarez, P., and C. Shene**. 1996. Experimental study of the heat and mass transfer during drying in a fluidized-bed dryer. *Drying Tech*. **14**(3-4): 701-718.
3. **Andersson, M., S. Folestad, J. Gottfires, M.O. Johansson, M. Josefson, and K.G. Wahlund.** 2000. Quantitative analysis of film coating in a fluidized-bed process by in-line NIR spectrometry and multivariate batch calibration. *Anal. Chem*. **72**: 2099-2108.
4. **Asif, M.** 2002a. Predicting binary solid fluidized-bed behavior using averaging approaches. *Powder Tech*. **127**: 226-238.
5. **Asif, M., and A.A. Ibrahim**. 2002b. Minimum fluidization velocity and de-fluidization behavior of binary solid-liquid fluidized-beds. 2002. *Powder Tech*. **126**: 241-254.
6. **Asif, M., and J.N. Petersen**. 1993. Particle dispersion in a binary solid-liquid fluidized-bed. *AICHE J*. **39**(9): 1465-1471.
7. **Baker, C.G.J**. 1999. Predicting the energy consumption of continuous well-mixed fluidized-bed dryers from drying kinetic data. *Drying Tech*. **17**(7-8): 1533-1555.
8. **Barghi, S., C.L. Briens, and M.A. Bergougnou**. 2003. Mixing and segregation of binary mixtures of particles in liquid-solid fluidized-beds. *Powder Tech*. **131**: 223-233.
9. **Berntsson, O., T. Burger, S. Folestad, S. Danielsson, L.G. Kuhn, and J. Fricke**. 1999. Effective sample size in diffuse reflectance near-infrared spectrometry. *Anal. Chem*. **71**: 617-623.
10. **Berntsson, O., L.G. Danielsson, and S. Folestad**. 2001. Characterization of diffuse reflectance fiber optic probe sampling on moving solids using a Fourier transform near-infrared spectrometer. *Anal. Chim. Acta*. **431**: 125-131.

11. **Berntsson, O., L.G. Danielsson, M.O. Johansson, and S. Folestad**. 2000. Quantitative determination of content in binary powder mixtures using diffuse reflectance near-infrared spectrometry and multivariate analysis. *Anal. Chim. Acta.* **419**: 45-54.
12. **Berntsson, O., L.G. Danielsson, B. Lagerholm, and S. Folestad**. 2002. Quantitative in-line monitoring of powder blending by near-infrared reflection spectroscopy. *Powder Tech.* **123**: 185-193.
13. **Berntsson, O., G. Zackrisson, and G. Östling.** 1997. Determination of moisture in hard gelatin capsules using near-infrared spectroscopy: applications to at-line process control of pharmaceutics. *J. of Pharm. Biomed. Anal*. **15**: 895-900.
14. **Blanco, M., J. Coello, S. Maspoch, and N. Pou.** 2000. Development and validation of near-infrared method for the analytical control of a pharmaceutical preparation in three steps of the manufacturing process. *J. Anal. Chem*. **368**: 534-539.
15. **Blanco, M., J. Coello, A. Eustaquio, H. Iturriaga, and S. Maspoch.** 1999. Analytical control of pharmaceutical production steps by near-infrared reflectance spectroscopy. *Anal Chim Acta.* **302**: 237-246.
16. **Blanco, M. R. Gozález, and E. Bertran**. 2002. Monitoring powder blending in pharmaceutical processes by use of near-infrared spectroscopy. *Talanta.* **56**: 203-212.
17. **Botterill, J.S.M.** 1975. *Fluid-bed Heat Transfer*. Academic Press. London.
18. **Buchanan, B.R., M.A. Baxter, T.S. Chen, X.Z. Qin, and P. Robinson.** 1996. Use of near-infrared spectroscopy to evaluate an active film in a film coated tablet. *Pharm. Res*. **13**(4): 616-621.
19. **Buijs, K., and G. Choppin**. 1963. Near-infrared studies of the structure of water-I. Pure Water. *J. Chem. Phys*. **39**: 2035-2041.
20. **Callis, J., D. Illman, and B. Kowalski.** 1987. Process analytical chemistry. *Anal. Chem*. **17**: 473-480.
21. **Choppin, G., and K. Buijs**. 1963. Near-infrared studies of the structure of water-II. Ionic Solutions. *J. Chem. Phys*. **39**: 2042-2050.

22. **Cook, E.M, and H.D. Dumont**. 1991. *Process Drying Practice*. McGraw Hill, Inc. New York.
23. **Curcio, J., and C. Petty**. 1951. The near-infrared absorption spectrum of liquid water. *J. Optic. Soc. Am*. **41**: 302-304.
24. **Derksen, M.W.J., P.J.M. Van de Oetelaar, and F.A. Maris.** 1998. The use of near-infrared spectroscopy in the efficient prediction of a specification for the residual moisture content of a freeze-dried product. *J. Pharm. Biomed. Anal.* **17**: 473-480.
25. **Dittman, F.W.** 1977. How to classify a drying process. *Chem*. *Eng*. **1**: 106-108.
26. **Duckworth, J., and A. Springsteen.** 1998. *Applied Spectroscopy*. Academic Press. San Diego, CA.
27. **Epstein, N., and B.P. LeClair**. 1985. Liquid fluidization of binary particle mixtures II. Bed inversion. *Chem. Eng. Sci*. **40**(8): 1517-1526.
28. **Fong, A., and G.M. Hieftje**. 1995. Near-infrared measurement of relative and absolute humidity through detection of water adsorbed on a silica gel layer. *Anal. Chem*. **67**: 1139-1146.
29. **Forina, M., M.C. Casolino, and C.P. Martínez.** 1998. Multivariate calibration: application to pharmaceutical analysis. *J. Pharm. Biomed. Anal*. **18**: 21-33.
30. **Frake, P., D. Greenhalgh, S.M. Grierson, J.M. Hempenstall, and D.R. Rudd**. 1997. Process control and end-point determination of a fluid-bed granulation by application of near-infrared spectroscopy. *Int. J. Pharm*. **151**: 75-80.
31. **Gelperin, N.I., and V.G. Einstein.** 1972. *Heat Transfer in Fluidized Beds*. Academic Press. London.
32. **Gibilaro, L.G., I. Hossain, and S.P. Waldram**. 1985. On the Kennedy and Bretton model for the mixing and segregation in liquid fluidized-beds. *Chem. Eng. Sci*. **40**(12): 2333-2338.
33. **Hailey, P.A., P. Doherty, P. Tapsell, T. Oliver, and P.K. Aldridge.** 1996. Automated system for the on-line monitoring of powder blending processes using near-infrared spectroscopy, Part I. System development and control. *J. Pharm. Biomed. Anal*. **14**: 551-559.

34. **Harris, S.C., and D.S. Walker.** 2000. Quantitative real-time monitoring of dryer effluent using fiber optic near-infrared spectroscopy. *J. Pharm. Sci.* **89**(9): 1180-1185.

35. **Hassel, D., and E. Bowman.** 1998. Process analytical chemistry for spectroscopists. *Appl. Spectrosc.* **52**: 18A-29A.

36. **Herschel, W.** 1800. Investigation of the powers of the prismatic colors to heat and illuminate objects; with remarks, that prove the different refrangibility of radiant heat. *Phil. Trans. of Roy. Soc.* **90**: 255-283.

37. **Keith, J.** 1980. *Particulate Science and Technology*. Chemical Publishing, Co. New York.

38. **Kirsch, J.D., and J.K. Drennen.** 1996. Near-infrared spectroscopy monitoring of the film coating process. *Pharm. Res.* **13**(2): 234-237.

39. **Langrish, T.A.G., and A.C. Harvey**. 2000. A flowsheet model of a well-mixed fluidized-bed dryer: application in controllability assessment and optimization. *Drying Tech.* **18**(1-2): 185-198.

40. **Liptak, B.** 1998. Optimizing dryer performance through better control. *Chem. Eng.* **2**: 110-114.

41. **McDonald, B.F., and K.A. Prebble.** 1993. Some applications of near-infrared reflectance analysis in the pharmaceutical industry. *J. Pharm & Biomed Anal.* **11**(11-12): 1077-1085.

42. **Mihura, B.** 2001. *LabVIEW for Data Acquisition*. Prentice Hall, Inc. New Jersey.

43. **Miwa, A., T. Yajima, and S. Itai.** 2000. Prediction of suitable amount of water addition for wet granulation. *Int. J. Pharm.* **195**: 81-92.

44. **Montgomery, D.C.** 2001. *Design and Analysis of Experiments.* Wiley & Sons, Inc. USA. 5th ed.

45. **Moreno, W.T.** 1993. *Aplicación al Diseño y Análisis de Experimentos.* Ediciones UIS. Bucaramanga, Colombia.

46. **Morris, K.R., J.G. Stowell, S.R. Byrn, A.W. Placette, T.D. Davis, and G.E. Peck.** 2000. Accelerated fluid-bed drying using NIR monitoring and phenomenological modeling. *Drug Dev & Ind Pharm.* **26**(9): 985-988.

47. **Morisseau, K.M., and C.T. Rhodes.** 1997. Near-infrared spectroscopy as a non-destructive alternative to conventional tablet hardness testing. *Pharm. Res.* **14**(1): 108-111.

48. **Mujundar, Arun S.** 1987. *Handbook of Industrial Drying*. Marcell Dekker, Inc. USA.

49. **Nomikos, P. and J. MacGregor**. 1995. Multivariate PSC charts for minitoring of batch processes. *Technometrics*. **37**: 41-59.

50. **Norris, K. and P. Williams**. 1983. Optimization of mathematical treatment of raw near-infrared signal in the measurement of protein in hard red spring wheat-I. Influence of particle size. *Cereal Chem*. **61**: 158-165.

51. **Osborne, B.G., T. Fearn, and P.H. Hindle.** 1993. *In Practical NIR Spectroscopy with Applications in Food Beverage Industry Analysis.* Longman, Harlow, UK. 2nd ed.

52. **Pasikatan, M.C., J.L. Steele, C.K. Spillman, and E. Haque**. 2001. Near-infrared reflectance spectroscopy for on-line particle size analysis of powders and ground materials. *J. Near Infrared Spectrosc*. **9**: 153-164.

53. **Popó, M., S. Romero, C. Conde, and R.J. Romañach**. 2002. Blend uniformity analysis using stream sampling and near-infrared spectroscopy. *AAPS Pharm Sci Tech*. **3**(3): 1-11.

54. **Rantanen, J., O. Antikanen, J.P. Mannermaa, and J. Yliruusi.** 2000. Use of near-infrared reflectance method for measurement of moisture content during granulation. *Pharm. Dev. Technol.* **5**(2): 209-217.

55. **Rantanen, J., S. Lehtola, P. Rämet, J.P. Mannermaa, and J. Yliruusi.** 1998. On-line monitoring of moisture content in a instrumented fluidized bed granulator with a multi-channel NIR moisture sensor. *Powder Technol*. **99**: 163-170.

56. **Reeves, J.** 1994. Effects of water on the spectra of model compounds in the short-wavelength near-infrared spectral region. *J. Near-Infrared Spectrosc*. **2**: 199.

57. **Seborg, D.E, T.F Edgar, and D.A. Mellichamp.** 1989. *Process Dynamics and Control*. Wiley & Sons. USA.

58. **Sekulic, S.S., J. Wakeman, P. Doherty, and P.A. Hailey.** 1998. Automated system for the on-line monitoring of powder blending process using neat-infrared spectroscopy, Part II. Qualitative approaches to blend evaluation. *J. Pharm. Biomed. Anal*. **17**: 1285-1309.

59. **Sekulic, S.S., H.W. Ward, D.R. Brannegan, E.D. Stanley, C.L. Evans, S.T. Sciavolino, P.A. Hailey, and P.K. Aldridge**. 1996. On-line monitoring of powder blend homogeneity by near-infrared spectroscopy. *Anal. Chem*. **68**: 509-513.

60. **Siesler, H.W., Y. Ozaki, S. Kawata, and H.M. Heise**. 2002. *Near-Infrared Spectroscopy: Principles, Instruments and Applications.* Wiley. Weinheim (Germany).

61. **Siettos, C.I., C.T. Kiranoudis, and G.V. Bafas**. 1999. Advanced control strategies for fluidized-bed dryers. *Drying Tech*. **17**(10): 2271-2291.

62. **Sinsheimer, J., and N. Poswalk**. 1968. Pharmaceutical applications of the near-infrared determination of water. *J. Pharm. Sci*. **57**: 2007-2010.

63. **Smith, C.A, and A.B. Corripio**. 1997. *Principles and Practice of Automatic Process Control*. Wiley & Sons. USA. 2nd ed.

64. **Soyemi, O.O., M.A. Busch, and K.W. Busch**. 2000. Multivariate analysis of near-infrared spectra using G-programming language. *J. Chem. Inf. Comput. Sci*. **40**: 1093-1100.

65. **Srinivasa, C., P.P. Thomas, and Y.B.G. Varma**. 1995. Drying of solids in fluidized-beds. *Ind. Eng. Chem. Res*. **34**: 3068-3077.

66. **Szentmarjay, T., A. Szalay, E. Pallai, T. Bencze, and J. Vass.** 1996. Control of drying process in mechanically spouted bed dryer. *Drying Tech*. **14**(3-4): 501-512.

67. **Tanfara, H., T. Pugsley, and C. Winters**. 2002. Effect of particle size distribution on local voidage in a bench-scale conical fluidized-bed dryer. *Drying Tech*. **20**(6): 1273-1289.

68. **Travis, J.** 2002. *LabVIEW for Everyone*. Prentice Hall, Inc. New Jersey. 2nd ed.

69. **Wang, Z. H., and G. Chen**. 2000. Heat and mass transfer in batch fluidized-bed drying of porous particles. *Chem. Eng. Sci*. **55**:1857-1869.

70. **Wetzel, D.L.** 1983. Near-infrared reflectance analysis: Sleeper among spectroscopic techniques. *Anal. Chem*. **55**(12): 1165A-1175A.

71. **Wold, S., N. Kettaneh, H. Fridén, and A. Holmberg**. 1998. Modelling and diagnostics of batch processes and analogous kinetic experiments. *Chemomet. Intell. Lab. Sys*. **44**: 331-340.

72. **Workman, J.J.** 1999a. Review of process and non-invasive near-infrared and infrared spectroscopy: 1993-1999. *Appl. Spectrosc. Rev*., **34**: 1-89.

73. **Workman, J.J., D. Veltkamp, S. Doherty, B. Anderson, K. Creasy, M. Koch, J. Tatera, A. Robinson, L. Bond, L. Burgess, G. Bokerman, A. Ullman, G. Darsey, F. Mozayeni, J. Bamberger, and M. Greenwood**. 1999b. Process analytical chemistry. *Anal. Chem*. **71**: 121R-180R.

74. **Wu, S.Y., and J. Baeyens**. 1998. Segregation by size difference in gas fluidized-beds. *Powder Tech*. **98**: 139-150.

75. **Zabrodsky, S.S.** 1966. *Hydrodynamics and Heat Transfer in Fluidized Beds*. MIT Press. Massachusetts.

APPENDICES

Appendix A: Additional Information for NIR Calibration Model

Table 10. Cross-Validation Report for the NIR Model Using 48 Samples

Validation Report

General Information

Method File:	calibracion(no pret).q2
Standards (total):	48
Calibration Spectra:	48
Test Spectra:	0
Data Block:	AB
Compounds (total):	1
Frequency Regions	1
Selected Datapoints:	624
Preprocessing:	No Spectral Data Preprocessing

Frequency Regions

from	to			
9002.7	4196.6			

moisture

Compound Range:	5.03 - 14.13
Compound Unit:	%
Validation Type:	Cross Validation
No. of samples leaving out:	1

Continuation of Cross-Validation Report for the NIR Model Using 48 Samples

Mean Prediction Error

Rank	R^2	RMSECV	Rec. Rank	
1	61.16	1.99		
2	88.88	1.07		
3	97.44	0.511		
4	97.43	0.513		
5	97.63	0.492	+	
6	97.79	0.475		
7	97.77	0.478		
8	97.5	0.506		
9	98.05	0.446		
10	97.88	0.466		

Compound Values

Used Rank: 5

	Filename	True	Prediction	Difference	Possible Outl
1	Av.2.2.0a	13.21	12.89	0.324	
2	Av.2.2.0b	13.42	12.51	0.913	
3	Av.2.2.0c	12.97	12.46	0.512	
4	Av.2.2.15a	5.41	6.117	-0.707	
5	Av.2.2.15b	5.35	5.947	-0.597	
6	Av.2.2.15c	5.72	6.269	-0.549	
7	Av.2.2.25a	5.09	5.903	-0.813	
8	Av.2.2.25b	5.15	5.853	-0.703	
9	Av.2.2.25c	5.03	5.668	-0.638	
10	Av.2.2.5a	10.05	10.27	-0.216	
11	Av.2.2.5b	9.79	10.37	-0.576	
12	Av.2.2.5c	10.44	10.53	-0.0851	
13	Av.3.3.0a	13.59	13.81	-0.223	
14	Av.3.3.0b	13.75	13.73	0.0169	
15	Av.3.3.0c	14.13	13.56	0.571	
16	Av.3.3.14a	5.88	6.021	-0.141	
17	Av.3.3.14b	6.26	5.76	0.5	
18	Av.3.3.14c	6.06	5.798	0.262	
19	Av.3.3.21a	5.48	5.606	-0.126	
20	Av.3.3.21b	5.55	5.418	0.132	
21	Av.3.3.21c	5.38	5.662	-0.282	
22	Av.3.3.7a	10.17	10.59	-0.416	
23	Av.3.3.7b	10.13	9.555	0.575	
24	Av.3.3.7c	10.3	9.978	0.322	
25	Av.4.4.0a	13.54	12.83	0.713	
26	Av.4.4.0b	12.85	13.36	-0.51	
27	Av.4.4.0c	12.8	13.58	-0.779	
28	Av.4.4.13a	5.26	5.8	-0.54	
29	Av.4.4.13b	6.32	5.608	0.712	
30	Av.4.4.13c	5.9	5.731	0.169	
31	Av.4.4.3a	10.61	10.94	-0.334	
32	Av.4.4.3b	10.56	10.93	-0.367	
33	Av.4.4.3c	10.46	10.82	-0.358	
34	Av.4.4.8a	7.36	6.812	0.548	

Continuation of Cross-Validation Report for the NIR Model Using 48 Samples

35	Av.4.4.8b	6.74	6.879	-0.139
36	Av.4.4.8c	6.65	6.878	-0.228
37	Av.5.5.0a	13.4	13.28	0.125
38	Av.5.5.0b	13.1	13.2	-0.1
39	Av.5.5.0c	13.15	13.34	-0.187
40	Av.5.5.10.a	5.79	5.534	0.256
41	Av.5.5.10b	5.78	5.538	0.242
42	Av.5.5.10c	5.77	5.543	0.227
43	Av.5.5.20a	6.63	5.389	1.24
44	Av.5.5.20b	5.61	5.605	0.00458
45	Av.5.5.20c	5.71	5.669	0.041
46	Av.5.5.5a	7.32	7.619	-0.299
47	Av.5.5.5b	8.21	7.206	1
48	Av.5.5.5c	7.35	7.088	0.262

Table 11. Calibration Report for the NIR Model Using 48 Samples

Calibration Report

General Information

Method File:	calibracion(no pret).q2
Standards (total):	48
Calibration Spectra:	48
Test Spectra:	0
Data Block:	AB
Compounds (total):	1
Frequency Regions	1
Selected Datapoints:	624
Preprocessing	No Spectral Data Preprocessing

Frequency Regions

from	to			
9002.7	4196.6			

moisture

Compound Range:	5.03 - 14.13
Compound Unit:	%

Continuation of Calibration Report for the NIR Model Using 48 Samples

Mean Estimation Error

Rank	R^2	RMSEE		
1	63.73	1.97		
2	90.46	1.02		
3	97.88	0.486		
4	98.25	0.447		
5	98.43	0.428		
6	98.57	0.414		
7	98.67	0.404		
8	99.19	0.32		
9	99.32	0.297		
10	99.45	0.271		

Compound Values

Used Rank: 5

	Filename	True	Fit	Residuum	Possible Outl
1	Av.2.2.0a	13.21	12.86	0.353	
2	Av.2.2.0b	13.42	12.83	0.593	
3	Av.2.2.0c	12.97	12.64	0.327	
4	Av.2.2.15a	5.41	5.967	-0.557	
5	Av.2.2.15b	5.35	5.747	-0.397	
6	Av.2.2.15c	5.72	6.061	-0.341	
7	Av.2.2.25a	5.09	5.787	-0.697	
8	Av.2.2.25b	5.15	5.652	-0.502	
9	Av.2.2.25c	5.03	5.588	-0.558	
10	Av.2.2.5a	10.05	10.19	-0.144	
11	Av.2.2.5b	9.79	10.25	-0.456	
12	Av.2.2.5c	10.44	10.41	0.0273	
13	Av.3.3.0a	13.59	13.78	-0.189	
14	Av.3.3.0b	13.75	13.76	-0.0102	
15	Av.3.3.0c	14.13	13.68	0.45	
16	Av.3.3.14a	5.88	6.001	-0.121	
17	Av.3.3.14b	6.26	5.828	0.432	
18	Av.3.3.14c	6.06	5.829	0.231	
19	Av.3.3.21a	5.48	5.583	-0.103	
20	Av.3.3.21b	5.55	5.439	0.111	
21	Av.3.3.21c	5.38	5.608	-0.228	
22	Av.3.3.7a	10.17	10.5	-0.328	
23	Av.3.3.7b	10.13	9.677	0.453	
24	Av.3.3.7c	10.3	10.04	0.258	
25	Av.4.4.0a	13.54	13.09	0.449	
26	Av.4.4.0b	12.85	13.27	-0.423	
27	Av.4.4.0c	12.8	13.49	-0.686	
28	Av.4.4.13a	5.26	5.75	-0.49	
29	Av.4.4.13b	6.32	5.693	0.627	
30	Av.4.4.13c	5.9	5.751	0.149	
31	Av.4.4.3a	10.61	10.9	-0.294	
32	Av.4.4.3b	10.56	10.88	-0.315	
33	Av.4.4.3c	10.46	10.79	-0.327	
34	Av.4.4.8a	7.36	6.898	0.462	

Continuation of Calibration Report for the NIR Model Using 48 Samples

35	Av.4.4.8b	6.74	6.861	-0.121	
36	Av.4.4.8c	6.65	6.854	-0.204	
37	Av.5.5.0a	13.4	13.3	0.104	
38	Av.5.5.0b	13.1	13.17	-0.0745	
39	Av.5.5.0c	13.15	13.27	-0.124	
40	Av.5.5.10.a	5.79	5.557	0.233	
41	Av.5.5.10b	5.78	5.565	0.215	
42	Av.5.5.10c	5.77	5.565	0.205	
43	Av.5.5.20a	6.63	5.518	1.11	*
44	Av.5.5.20b	5.61	5.606	0.00438	
45	Av.5.5.20c	5.71	5.679	0.0312	
46	Av.5.5.5a	7.32	7.541	-0.221	
47	Av.5.5.5b	8.21	7.35	0.86	
48	Av.5.5.5c	7.35	7.128	0.222	

Table 12. Cross-Validation Report for the NIR Model with No-Outliers

Validation Report

General Information

Method File:	calibracion(no pret).q2
Standards (total):	48
Calibration Spectra:	47
Test Spectra:	0
Data Block:	AB
Compounds (total):	1
Frequency Regions	1
Selected Datapoints:	624
Preprocessing:	No Spectral Data Preprocessing

Frequency Regions

from	to				
9002.7	4196.6				

moisture

Compound Range:	5.03 - 14.13
Compound Unit:	%
Validation Type:	Cross Validation
No. of samples leaving out:	1

Continuation of Cross-Validation Report for the NIR Model with No-Outliers

Mean Prediction Error

Rank	R^2	RMSECV	Rec. Rank	
1	60.92	2.01		
2	88.84	1.08		
3	97.86	0.471		
4	97.8	0.477		
5	98.05	0.449	+	
6	98.15	0.438		
7	98.06	0.449		
8	97.8	0.478		
9	98.25	0.426		
10	98.04	0.45		

Compound Values

Used Rank: 5

	Filename	True	Prediction	Difference	Possible Outl
1	Av.2.2.0a	13.21	12.98	0.228	
2	Av.2.2.0b	13.42	12.43	0.991	
3	Av.2.2.0c	12.97	12.62	0.354	
4	Av.2.2.15a	5.41	6.118	-0.708	
5	Av.2.2.15b	5.35	5.891	-0.541	
6	Av.2.2.15c	5.72	6.129	-0.409	
7	Av.2.2.25a	5.09	5.876	-0.786	
8	Av.2.2.25b	5.15	5.709	-0.559	
9	Av.2.2.25c	5.03	5.602	-0.572	
10	Av.2.2.5a	10.05	10.23	-0.183	
11	Av.2.2.5b	9.79	10.4	-0.613	
12	Av.2.2.5c	10.44	10.52	-0.0826	
13	Av.3.3.0a	13.59	13.85	-0.258	
14	Av.3.3.0b	13.75	13.74	0.0122	
15	Av.3.3.0c	14.13	13.57	0.559	
16	Av.3.3.14a	5.88	6.006	-0.126	
17	Av.3.3.14b	6.26	5.768	0.492	
18	Av.3.3.14c	6.06	5.814	0.246	
19	Av.3.3.21a	5.48	5.582	-0.102	
20	Av.3.3.21b	5.55	5.388	0.162	
21	Av.3.3.21c	5.38	5.62	-0.24	
22	Av.3.3.7a	10.17	10.58	-0.41	
23	Av.3.3.7b	10.13	9.634	0.496	
24	Av.3.3.7c	10.3	10.03	0.273	
25	Av.4.4.0a	13.54	12.85	0.687	
26	Av.4.4.0b	12.85	13.32	-0.472	
27	Av.4.4.0c	12.8	13.57	-0.771	
28	Av.4.4.13a	5.26	5.711	-0.451	
29	Av.4.4.13b	6.32	5.612	0.708	
30	Av.4.4.13c	5.9	5.646	0.254	
31	Av.4.4.3a	10.61	10.98	-0.372	
32	Av.4.4.3b	10.56	10.96	-0.397	
33	Av.4.4.3c	10.46	10.82	-0.361	
34	Av.4.4.8a	7.36	6.843	0.517	

Continuation of Cross-Validation Report for the NIR Model with No-Outliers

35	Av.4.4.8b	6.74	6.854	-0.114
36	Av.4.4.8c	6.65	6.861	-0.211
37	Av.5.5.0a	13.4	13.27	0.131
38	Av.5.5.0b	13.1	13.18	-0.0804
39	Av.5.5.0c	13.15	13.3	-0.153
40	Av.5.5.10.a	5.79	5.446	0.344
41	Av.5.5.10b	5.78	5.493	0.287
42	Av.5.5.10c	5.77	5.495	0.275
44	Av.5.5.20b	5.61	5.52	0.0901
45	Av.5.5.20c	5.71	5.561	0.149
46	Av.5.5.5a	7.32	7.617	-0.297
47	Av.5.5.5b	8.21	7.168	1.04
48	Av.5.5.5c	7.35	7.063	0.287

Table 13. Calibration Report for the NIR Model with No-Outliers

Calibration Report

General Information

Method File:	calibracion(no pret).q2
Standards (total):	48
Calibration Spectra:	47
Test Spectra:	0
Data Block:	AB
Compounds (total):	1
Frequency Regions	1
Selected Datapoints:	624
Preprocessing	No Spectral Data Preprocessing

Frequency Regions

from	to			
9002.7	4196.6			

moisture

Compound Range:	5.03 - 14.13
Compound Unit:	%

Continuation of Calibration Report for the NIR Model with No-Outliers

Mean Estimation Error

Rank	R^2	RMSEE		
1	63.55	1.99		
2	90.44	1.03		
3	98.23	0.447		
4	98.54	0.412		
5	98.68	0.396		
6	98.77	0.388		
7	98.87	0.375		
8	99.32	0.295		
9	99.45	0.27		
10	99.54	0.25		

Compound Values

Used Rank: 5

	Filename	True	Fit	Residuum	Possible Outl
1	Av.2.2.0a	13.21	12.83	0.381	
2	Av.2.2.0b	13.42	12.76	0.659	
3	Av.2.2.0c	12.97	12.66	0.314	
4	Av.2.2.15a	5.41	5.97	-0.56	
5	Av.2.2.15b	5.35	5.719	-0.369	
6	Av.2.2.15c	5.72	5.916	-0.196	
7	Av.2.2.25a	5.09	5.758	-0.668	
8	Av.2.2.25b	5.15	5.505	-0.355	
9	Av.2.2.25c	5.03	5.528	-0.498	
10	Av.2.2.5a	10.05	10.19	-0.143	
11	Av.2.2.5b	9.79	10.26	-0.475	
12	Av.2.2.5c	10.44	10.41	0.0286	
13	Av.3.3.0a	13.59	13.8	-0.209	
14	Av.3.3.0b	13.75	13.75	-0.00101	
15	Av.3.3.0c	14.13	13.69	0.438	
16	Av.3.3.14a	5.88	6.004	-0.124	
17	Av.3.3.14b	6.26	5.838	0.422	
18	Av.3.3.14c	6.06	5.846	0.214	
19	Av.3.3.21a	5.48	5.559	-0.0787	
20	Av.3.3.21b	5.55	5.417	0.133	
21	Av.3.3.21c	5.38	5.575	-0.195	
22	Av.3.3.7a	10.17	10.55	-0.382	
23	Av.3.3.7b	10.13	9.755	0.375	
24	Av.3.3.7c	10.3	10.11	0.187	
25	Av.4.4.0a	13.54	13.07	0.466	
26	Av.4.4.0b	12.85	13.25	-0.399	
27	Av.4.4.0c	12.8	13.47	-0.673	
28	Av.4.4.13a	5.26	5.672	-0.412	
29	Av.4.4.13b	6.32	5.64	0.68	
30	Av.4.4.13c	5.9	5.671	0.229	
31	Av.4.4.3a	10.61	10.94	-0.329	
32	Av.4.4.3b	10.56	10.91	-0.346	
33	Av.4.4.3c	10.46	10.79	-0.331	
34	Av.4.4.8a	7.36	6.932	0.428	

Continuation of Calibration Report for the NIR Model with No-Outliers

35	Av.4.4.8b	6.74	6.84	-0.1
36	Av.4.4.8c	6.65	6.841	-0.191
37	Av.5.5.0a	13.4	13.29	0.109
38	Av.5.5.0b	13.1	13.16	-0.0607
39	Av.5.5.0c	13.15	13.25	-0.101
40	Av.5.5.10.a	5.79	5.45	0.34
41	Av.5.5.10b	5.78	5.463	0.317
42	Av.5.5.10c	5.77	5.465	0.305
44	Av.5.5.20b	5.61	5.503	0.107
45	Av.5.5.20c	5.71	5.563	0.147
46	Av.5.5.5a	7.32	7.541	-0.221
47	Av.5.5.5b	8.21	7.32	0.89
48	Av.5.5.5c	7.35	7.1	0.25

Table 14. Opus Software Specifications for NIR Acquisition of Spectra

Acquisition Parameters	
Description	**Value**
Acquisition Mode	Double Sided, Forward-Backward
Correlation Test Mode	No
Delay Before Measurement	0
Resolution	16
Result Spectrum	Absorbance
Sample Scans	32
Signal Gain, Background	Automatic
Signal Gain, Sample	Automatic
Stabilization Delay	0
Wanted High Frequency Limit	15000
Wanted Low Frequency Limit	0
Fourier Transform Parameters	
Description	**Value**
Apodization Function	Blackman-Harris 3-Term
End Frequency Limit for File	4000
Start Frequency Limit for File	12000
Phase Resolution	128
Phase Correction Mode	Mertz
Stored Phase Mode	No
Zero Filling Factor	2
Optics Parameters	
Description	**Value**
Aperture Setting	Open
Measurement Channel	Fiber 1
Detector Setting	429 (InGaAs)
Low Pass Filter	1 ; 10 KHz
Preamplifier Gain	1
Source Setting	Tungsten (NIR)
Scanner Velocity	6 ; 10.0 KHz
Instrument Parameters	
Description	**Value**
High Folding Limit	15799.07
Low Folding Limit	0

Continuation of Opus Software Specifications for NIR Acquisition of Spectra

Laser Wavenumber	15799.07
Absolute Peak Pos in Laser*2	60718
Sample Spacing Divisor	1
Actual Signal Gain	8
Switch Gain Position	763
Gain Switch Window	250
Scan time (sec)	13.25
Peak Amplitude	3209
Peak Location	1764
Number of Good FW Scans	16
Backward Peak Amplitude	3241
Backward Peak Location	1790
Number of Good BW Scans	16
Instrument Type	VECTOR22N
Number of Sample Scans	32
Number of Background Scans	32
Running Sample Number	932

Appendix B: Additional Information for ANOVA Analysis

Table 15. ANOVA Relations for Three Factor Factorial Design

Source	Sum of Squares	Degrees of Freedom	Mean Square	F Value
A	$SS_A = \sum_i^a \frac{Y_i^2\cdots}{bcn} - \frac{Y^2\cdots\cdot}{abcn}$	a-1	$MS_A = \frac{SS_A}{a-1}$	$\frac{MS_A}{MS_E}$
B	$SS_B = \sum_j^b \frac{Y^2\cdot_j\cdot\cdot}{acn} - \frac{Y^2\cdots\cdot}{abcn}$	b-1	$MS_B = \frac{SS_B}{b-1}$	$\frac{MS_B}{MS_E}$
C	$SS_C = \sum_k^c \frac{Y^2\cdot\cdot_k\cdot}{abn} - \frac{Y^2\cdots\cdot}{abcn}$	c-1	$MS_C = \frac{SS_C}{c-1}$	$\frac{MS_C}{MS_E}$
AB	$SS_{AB} = \sum_i^a \sum_j^b \frac{Y^2_{ij}\cdot\cdot}{cn} - \frac{Y^2\cdots\cdot}{abcn} - SS_A - SS_B$	(a-1)(b-1)	$MS_{AB} = \frac{SS_{AB}}{(a-1)(b-1)}$	$\frac{MS_{AB}}{MS_E}$
AC	$SS_{AC} = \sum_i^a \sum_k^c \frac{Y^2_{i\cdot k}\cdot}{bn} - \frac{Y^2\cdots\cdot}{abcn} - SS_A - SS_C$	(a-1)(c-1)	$MS_{AC} = \frac{SS_{AC}}{(a-1)(c-1)}$	$\frac{MS_{AC}}{MS_E}$
BC	$SS_{BC} = \sum_j^b \sum_k^c \frac{Y^2\cdot_{jk}\cdot}{an} - \frac{Y^2\cdots\cdot}{abcn} - SS_B - SS_C$	(b-1)(c-1)	$MS_{BC} = \frac{SS_{BC}}{(b-1)(c-1)}$	$\frac{MS_{BC}}{MS_E}$
ABC	$SS_{ABC} = \sum_i^a \sum_j^b \sum_k^c \frac{Y^2_{ijk}\cdot}{n} - \frac{Y^2\cdots\cdot}{abcn} - SS_A - SS_B - SS_C - SS_{AB} - SS_{AC} - SS_{BC}$	(a-1)(b-1)(c-1)	$MS_{ABC} = \frac{SS_{ABC}}{(a-1)(b-1)(c-1)}$	$\frac{MS_{ABC}}{MS_E}$
Error	$SS_E = SS_{TOTAL} - \sum_i^a \sum_j^b \sum_k^c \frac{Y^2_{ijk}\cdot}{n}$	abc(n-1)	$MS_E = \frac{SS_E}{abc(n-1)}$	
Total	$SS_{TOTAL} = \sum_i^a \sum_j^b \sum_k^c \sum^n Y^2_{ijkl} - \frac{Y^2\cdots\cdot}{abcn}$	abcn-1		

Table 16. ANOVA Report for Full Mixed-Level Factorial Using All Factors

Response: Residual
ANOVA for Selected Factorial Model
Analysis of variance table [Partial sum of squares]

Source	Sum of Squares	DF	Mean Square	F Value	Prob > F	
Block	0.83	1	0.83			
Model	17.09	17	1.01	13.38	< 0.0001	significant
A	*0.74*	*1*	*0.74*	*9.84*	*0.0060*	
B	*2.62*	*2*	*1.31*	*17.45*	*< 0.0001*	
C	*5.57*	*2*	*2.79*	*37.07*	*< 0.0001*	
AB	*0.26*	*2*	*0.13*	*1.75*	*0.2039*	
AC	*4.25*	*2*	*2.12*	*28.26*	*< 0.0001*	
BC	*3.10*	*4*	*0.78*	*10.32*	*0.0002*	
ABC	*0.54*	*4*	*0.14*	*1.80*	*0.1749*	
Residual	1.28	17	0.075			
Cor Total	19.20	35				

Continuation of ANOVA Report for Full Mixed-Level Factorial Using All Factors

The Model F-value of 13.38 implies the model is significant. There is only a 0.01% chance that a "Model F-Value" this large could occur due to noise.

Values of "Prob > F" less than 0.0500 indicate model terms are significant.
In this case A, B, C, AC, BC are significant model terms.
Values greater than 0.1000 indicate the model terms are not significant.
If there are many insignificant model terms (not counting those required to support hierarchy), model reduction may improve your model.

Std. Dev.	0.27	R-Squared	0.9304
Mean	-1.11	Adj R-Squared	0.8609
C.V.	-24.76	Pred R-Squared	0.6880
PRESS	5.73	Adeq Precision	11.720

The "Pred R-Squared" of 0.6880 is in reasonable agreement with the "Adj R-Squared" of 0.8609.

"Adeq Precision" measures the signal to noise ratio. A ratio greater than 4 is desirable. Your ratio of 11.720 indicates an adequate signal. This model can be used to navigate the design space.

Term	**Coefficient Estimate**	**DF**	**Standard Error**	**95% CI Low**	**95% CI High**	**VIF**
Intercept	-1.11	1	0.046	-1.20	-1.01	
Lot 1	-0.15	1				
Lot 2	0.15					
A-Mass Load	-0.14	1	0.046	-0.24	-0.047	1.00
B[1]	-0.37	1	0.065	-0.51	-0.23	
B[2]	0.10	1	0.065	-0.032	0.24	
C[1]	-0.34	1	0.065	-0.47	-0.20	
C[2]	0.55	1	0.065	0.42	0.69	
AB[1]	0.059	1	0.065	-0.077	0.20	
AB[2]	-0.12	1	0.065	-0.26	0.016	
AC[1]	-0.49	1	0.065	-0.62	-0.35	
AC[2]	0.25	1	0.065	0.11	0.38	
B[1]C[1]	0.31	1	0.091	0.11	0.50	
B[2]C[1]	0.11	1	0.091	-0.088	0.30	
B[1]C[2]	0.19	1	0.091	-2.542E-003	0.38	
B[2]C[2]	-0.19	1	0.091	-0.38	5.597E-003	
AB[1]C[1]	-0.085	1	0.091	-0.28	0.11	
AB[2]C[1]	-0.12	1	0.091	-0.32	0.070	
AB[1]C[2]	0.14	1	0.091	-0.052	0.33	
AB[2]C[2]	0.058	1	0.091	-0.13	0.25	

Final Equation in Terms of Coded Factors:

Residual	=
-1.11	
-0.14	* A
-0.37	* B[1]
+0.10	* B[2]
-0.34	* C[1]
+0.55	* C[2]
+0.059	* AB[1]
-0.12	* AB[2]
-0.49	* AC[1]
+0.25	* AC[2]
+0.31	* B[1]C[1]
+0.11	* B[2]C[1]
+0.19	* B[1]C[2]
-0.19	* B[2]C[2]
-0.085	* AB[1]C[1]
-0.12	* AB[2]C[1]
+0.14	* AB[1]C[2]
+0.058	* AB[2]C[2]

Continuation of ANOVA Report for Full Mixed-Level Factorial Using All Factors

Final Equation in Terms of Actual Factors:

Not available, because this model contains more than 12 categorical equations.

Diagnostics Case Statistics

Standard Order	Actual Value	Predicted Value	Residual	Leverage	Outlier t	Run Order
1	-0.80	-1.00	0.20	0.528	1.078	5
2	-0.90	-0.70	-0.20	0.528	-1.078	25
3	-2.29	-2.31	0.022	0.528	0.114	1
4	-2.03	-2.01	-0.022	0.528	-0.114	23
5	-0.39	-0.51	0.12	0.528	0.637	14
6	-0.33	-0.21	-0.12	0.528	-0.637	36
7	-2.10	-2.26	0.16	0.528	0.827	10
8	-2.11	-1.95	-0.16	0.528	-0.827	29
9	-1.30	-1.38	0.082	0.528	0.426	6
10	-1.16	-1.08	-0.082	0.528	-0.426	30
11	-1.92	-2.10	0.18	0.528	0.965	3
12	-1.98	-1.80	-0.18	0.528	-0.965	20
13	-1.09	-1.19	0.10	0.528	0.531	13
14	-0.99	-0.89	-0.10	0.528	-0.531	19
15	-0.55	-0.58	0.032	0.528	0.166	18
16	-0.31	-0.28	-0.032	0.528	-0.166	27
17	-0.64	-0.83	0.19	0.528	1.022	2
18	-0.72	-0.53	-0.19	0.528	-1.022	32
19	-1.15	-0.75	-0.40	0.528	-2.425	9
20	-0.040	-0.44	0.40	0.528	2.425	26
21	-0.39	-0.41	0.022	0.528	0.114	16
22	-0.13	-0.11	-0.022	0.528	-0.114	24
23	-0.43	-0.48	0.047	0.528	0.244	15
24	-0.22	-0.17	-0.047	0.528	-0.244	22
25	-2.71	-2.44	-0.27	0.528	-1.469	11
26	-1.87	-2.14	0.27	0.528	1.469	28
27	-2.32	-2.25	-0.073	0.528	-0.376	4
28	-1.87	-1.94	0.073	0.528	0.376	34
29	-1.78	-1.33	-0.45	0.528	-2.869	7
30	-0.57	-1.02	0.45	0.528	2.869	31
31	-1.12	-1.25	0.13	0.528	0.691	17
32	-1.08	-0.95	-0.13	0.528	-0.691	21
33	-0.99	-0.94	-0.048	0.528	-0.246	12
34	-0.59	-0.64	0.048	0.528	0.246	33
35	-0.70	-0.65	-0.053	0.528	-0.272	8
36	-0.29	-0.34	0.053	0.528	0.272	35

Note: Predicted values include block corrections.

Table 17. ANOVA Report for Full Mixed-Level Factorial Using Only Significant Factors

Response: Residual

ANOVA for Selected Factorial Model

Analysis of variance table [Partial sum of squares]

Source	Sum of Squares	DF	Mean Square	F Value	Prob > F
Block	0.83	1	0.83		
Model	16.29	11	1.48	16.35	< 0.0001
significant					
A	*0.74*	*1*	*0.74*	*8.17*	*0.0089*
B	*2.62*	*2*	*1.31*	*14.48*	*< 0.0001*
C	*5.57*	*2*	*2.79*	*30.77*	*< 0.0001*
AC	*4.25*	*2*	*2.12*	*23.46*	*< 0.0001*
BC	*3.10*	*4*	*0.78*	*8.57*	*0.0002*

Continuation of ANOVA Report for Full Mixed-Level Factorial Using Only Significant Factors

Residual	2.08	23	0.091
Cor Total	19.20	35	

The Model F-value of 16.35 implies the model is significant. There is only a 0.01% chance that a "Model F-Value" this large could occur due to noise.

Values of "Prob > F" less than 0.0500 indicate model terms are significant.
In this case A, B, C, AC, BC are significant model terms.
Values greater than 0.1000 indicate the model terms are not significant.
If there are many insignificant model terms (not counting those required to support hierarchy), model reduction may improve your model.

Std. Dev.	0.30	R-Squared	0.8866
Mean	-1.11	Adj R-Squared	0.8324
C.V.	-27.18	Pred R-Squared	0.7222
PRESS	5.10	Adeq Precision	13.292

The "Pred R-Squared" of 0.7222 is in reasonable agreement with the "Adj R-Squared" of 0.8324.

"Adeq Precision" measures the signal to noise ratio. A ratio greater than 4 is desirable. Your ratio of 13.292 indicates an adequate signal. This model can be used to navigate the design space.

Term VIF	**Coefficient Estimate**	**DF**	**Standard Error**	**95% CI Low**	**95% CI High**
Intercept	-1.11	1	0.050	-1.21	-1.00
Lot 1	-0.15	1			
Lot 2	0.15				
A-Mass Load 1.00	-0.14	1	0.050	-0.25	-0.040
B[1]	-0.37	1	0.071	-0.52	-0.22
B[2]	0.10	1	0.071	-0.042	0.25
C[1]	-0.34	1	0.071	-0.48	-0.19
C[2]	0.55	1	0.071	0.41	0.70
AC[1]	-0.49	1	0.071	-0.63	-0.34
AC[2]	0.25	1	0.071	0.10	0.40
B[1]C[1]	0.31	1	0.10	0.10	0.52
B[2]C[1]	0.11	1	0.10	-0.10	0.31
B[1]C[2]	0.19	1	0.10	-0.017	0.40
B[2]C[2]	-0.19	1	0.10	-0.39	0.020

Final Equation in Terms of Coded Factors:

Residual	=
-1.11	
-0.14	* A
-0.37	* B[1]
+0.10	* B[2]
-0.34	* C[1]
+0.55	* C[2]
-0.49	* AC[1]
+0.25	* AC[2]
+0.31	* B[1]C[1]
+0.11	* B[2]C[1]
+0.19	* B[1]C[2]
-0.19	* B[2]C[2]

Final Equation in Terms of Actual Factors:

Not available, because this model contains more than 12 categorical equations.

Continuation of ANOVA Report for Full Mixed-Level Factorial Using Only Significant Factors

Diagnostics Case Statistics

Standard Order	Actual Value	Predicted Value	Residual	Leverage	Outlier t	Run Order
1	-0.80	-1.03	0.23	0.361	0.946	5
2	-0.90	-0.72	-0.18	0.361	-0.726	25
3	-2.29	-2.29	-3.611E-003	0.361	-0.015	1
4	-2.03	-1.98	-0.048	0.361	-0.196	23
5	-0.39	-0.76	0.37	0.361	1.567	14
6	-0.33	-0.45	0.12	0.361	0.495	36
7	-2.10	-2.01	-0.086	0.361	-0.351	10
8	-2.11	-1.71	-0.40	0.361	-1.737	29
9	-1.30	-1.11	-0.19	0.361	-0.770	6
10	-1.16	-0.81	-0.35	0.361	-1.500	30
11	-1.92	-2.37	0.45	0.361	1.994	3
12	-1.98	-2.07	0.087	0.361	0.355	20
13	-1.09	-0.99	-0.098	0.361	-0.399	13
14	-0.99	-0.69	-0.30	0.361	-1.273	19
15	-0.55	-0.78	0.23	0.361	0.964	18
16	-0.31	-0.48	0.17	0.361	0.690	27
17	-0.64	-0.89	0.25	0.361	1.062	2
18	-0.72	-0.59	-0.13	0.361	-0.531	32
19	-1.15	-0.68	-0.47	0.361	-2.068	9
20	-0.040	-0.38	0.34	0.361	1.448	26
21	-0.39	-0.55	0.16	0.361	0.656	16
22	-0.13	-0.25	0.12	0.361	0.471	24
23	-0.43	-0.34	-0.090	0.361	-0.368	15
24	-0.22	-0.035	-0.18	0.361	-0.761	22
25	-2.71	-2.44	-0.27	0.361	-1.134	11
26	-1.87	-2.13	0.26	0.361	1.105	28
27	-2.32	-2.25	-0.069	0.361	-0.283	4
28	-1.87	-1.95	0.076	0.361	0.310	34
29	-1.78	-1.38	-0.40	0.361	-1.715	7
30	-0.57	-1.08	0.51	0.361	2.309	31
31	-1.12	-1.20	0.076	0.361	0.308	17
32	-1.08	-0.89	-0.19	0.361	-0.779	21
33	-0.99	-0.89	-0.10	0.361	-0.413	12
34	-0.59	-0.58	-5.556E-003	0.361	-0.023	33
35	-0.70	-0.70	5.556E-004	0.361	0.002	8
36	-0.29	-0.40	0.11	0.361	0.433	35

Note: Predicted values include block corrections.

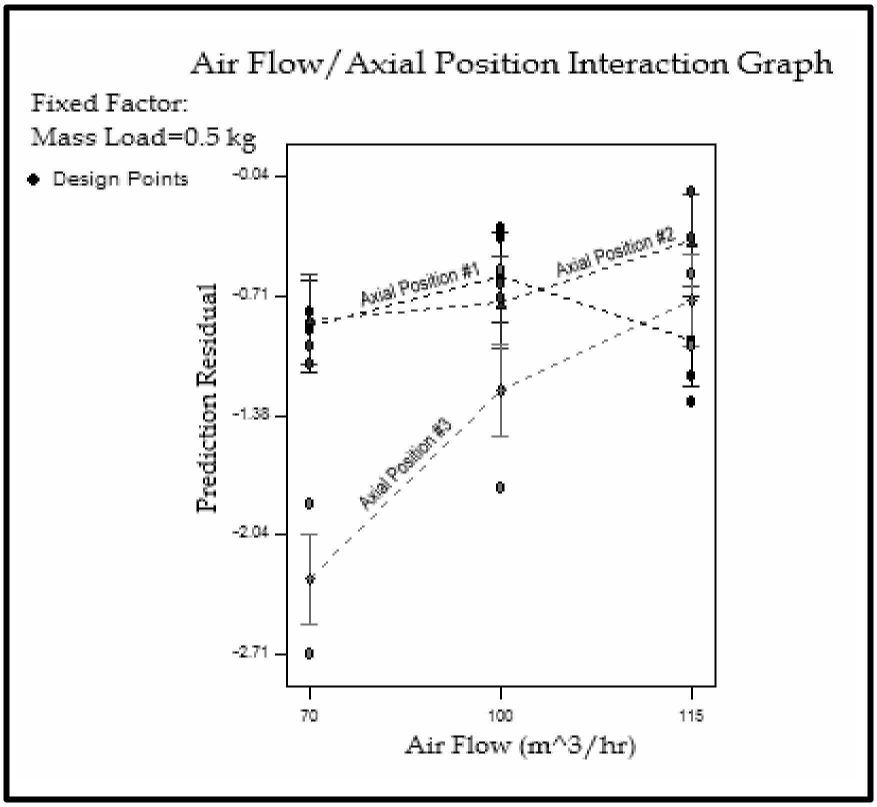

Figure 25. Plot of the air flow vs. axial position interaction effect for the lowest level of mass load

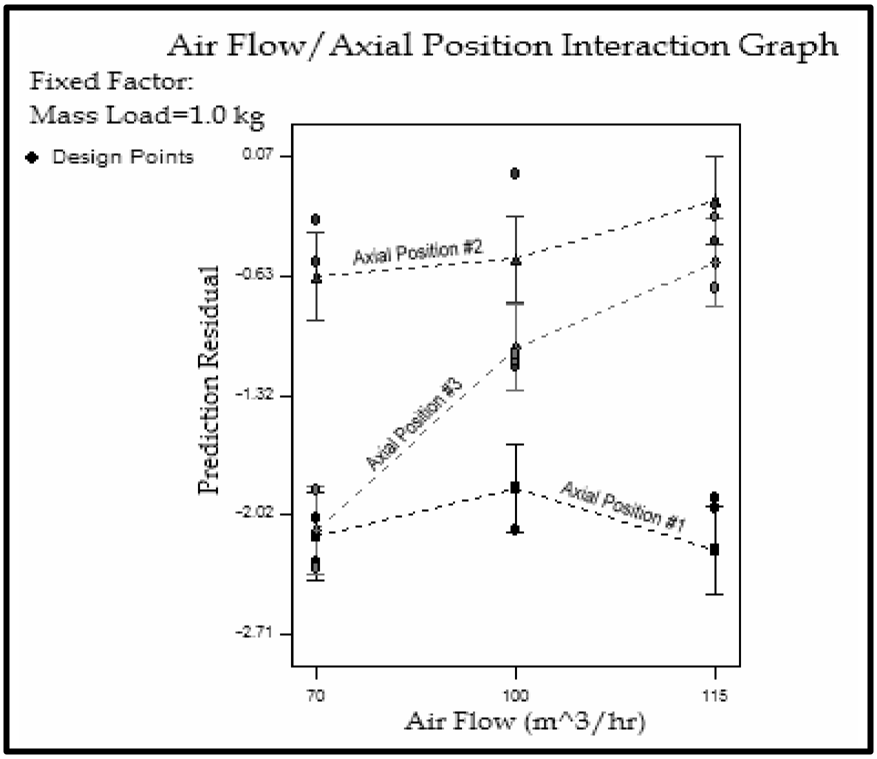

Figure 26. Plot of the air flow vs. axial position interaction effect for the highest level of mass load

Table 18. In-line and Static NIR Raw Moisture Data for Experimental Design

Block or Lot Number	[1]Treatment Combination	In-line NIR Value (%)	Static NIR Value (%)	Static NIR Average (%)	[2]Residual
1	000	6.43	5.74	5.63	-0.80
	001	6.72	5.55		-1.09
	002	8.34	5.61		-2.71
	010	6.02	5.85		-0.39
	011	6.27	5.57		-0.64
	012	7.41	5.50		-1.78
	020	6.93	5.71		-1.30
	021	6.02	5.59		-0.39
	022	6.62	5.68		-0.99
	100	7.84	5.50	5.55	-2.29
	101	6.10	5.50		-0.55
	102	7.87	5.59		-2.32
	110	7.65	5.57		-2.10
	111	6.70	5.51		-1.15
	112	6.67	5.51		-1.12
	120	7.47	5.78		-1.92
	121	5.98	5.54		-0.43
	122	6.25	5.49		-0.70
2	000	6.73	5.88	5.83	-0.90
	001	6.82	6.01		-0.99
	002	7.70	5.72		-1.87
	010	6.16	5.80		-0.33
	011	6.55	5.74		-0.72
	012	6.40	5.84		-0.57
	020	6.99	5.95		-1.16
	021	5.96	6.02		-0.13
	022	6.42	5.70		-0.59
	100	7.83	5.68	5.80	-2.03
	101	6.11	5.76		-0.31
	102	7.67	5.95		-1.87
	110	7.91	5.75		-2.11
	111	5.84	5.77		-0.04
	112	6.88	5.84		-1.08
	120	7.78	5.84		-1.98
	121	6.02	5.74		-0.22
	122	6.09	5.80		-0.29

[1] The sample names are coded with the following sequence: the first number indicates the levels of mass load (0 = 0.5kg and 1 = 1.5 kg). The same approached was taken for the second and third numbers that are the levels of air flow and probe position, respectively.

[2] The residuals shown here are the difference between the third and fifth columns. The negative signs are due to the fact that the static samples values were taken as the correct NIR prediction for the sample.

Appendix C: Additional Information for Application of Control

Table 19. List of Equipments for the Instrumentation and Control Panel

Softwares		
Equipment	**Manufacturer**	**Quantity**
LabVIEW® full version 6.0i	National Instruments™	1
Process Pro® version 2.7	Bruker Optics™	1
Opus® version 4.0	Bruker Optics™	1
Hardware		
Equipment	**Manufacturer**	**Quantity**
Type J thermocouples transition probes	Omega™ Engineering Co.	3
25 amp solid state relays model SSR240DC25 with heat sinks model FHS-2	Omega™ Engineering Co.	2
Pulse control module model PCM1	Omega™ Engineering Co.	1
Multifuntion I/O board model PCI-6025E	National Instruments™	1
16-channel backplane for signal conditioning series 5B model 776291-91	National Instruments™	1
Thermocouple type J input module model 5B47	National Instruments™	3
Current input module model 5B32	National Instruments™	1
Current output module model 5B39	National Instruments™	1
Electromechanical relay block model CB-50	National Instruments™	1
Cable adapter model SC-2050	National Instruments™	1
Ribbon cable model NB1	National Instruments™	1
Ribbon cable model NB7	National Instruments™	2
Ribbon cable model NB8	National Instruments™	1
Dual channel 12-bit analog output board model CIO-DAC02	Measurement Computing™ Co.	1
25-pin D male type connector cable model DMCON-25	Measurement Computing™ Co.	1

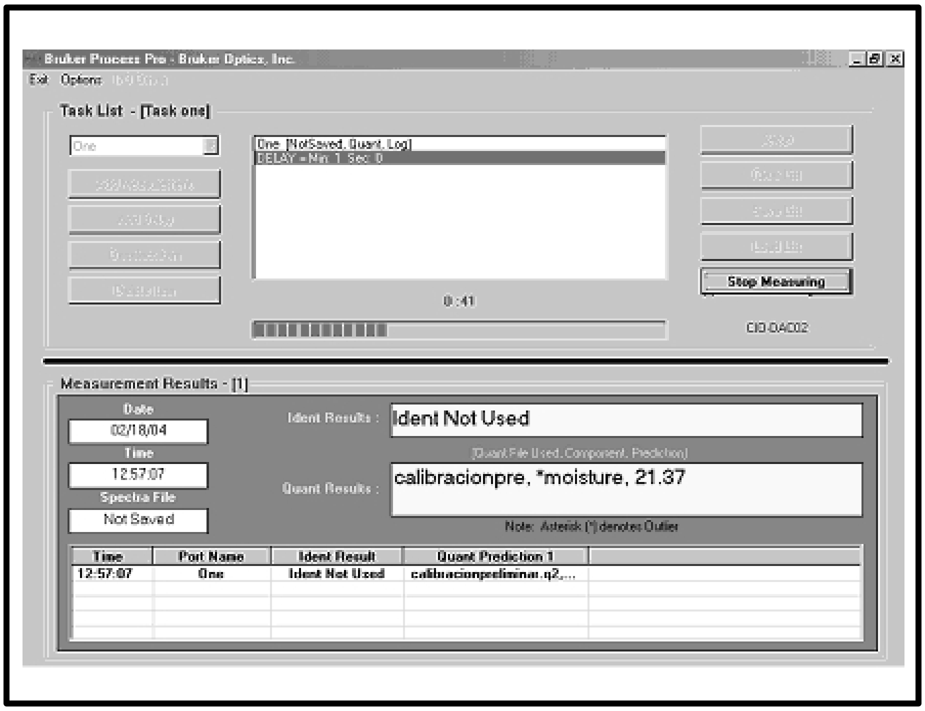

Figure 27. Process Pro graphical user interface